Additive manufactured versus cast AlSi10Mg alloy
Microstructure and micromechanics

Shakil, S. I.; Hadadzadeh, A.; Shalchi Amirkhiz, B.; Pirgazi, H.; Mohammadi, M.; Haghshenas, M.

DOI
10.1016/j.rinma.2021.100178

Publication date
2021

Document Version
Final published version

Published in
Results in Materials

Results in Materials 10 (2021) 100178

Contents lists available at ScienceDirect

Results in Materials

journal homepage: www.journals.elsevier.com/results-in-materials

Additive manufactured versus cast AlSi10Mg alloy: Microstructure and micromechanics

S.I. Shakil [a], A. Hadadzadeh [b], B. Shalchi Amirkhiz [c], H. Pirgazi [d,e], M. Mohammadi [f], M. Haghshenas [a,*]

[a] Micro/Nanomechanics Laboratory, Department of Mechanical, Industrial and Manufacturing Engineering, University of Toledo, Toledo, OH, USA
[b] Department of Mechanical Engineering, University of Memphis, Memphis, TN, USA
[c] CanmetMATERIALS, Natural Resources Canada, 183 Longwood Road South, Hamilton, ON, L8P 0A5, Canada
[d] Department of Electromechanical, Systems and Metal Engineering, Ghent University, Technologiepark 46, 9052, Zwijnaarde, Belgium
[e] Department of Materials Science and Engineering, Delft University of Technology, Mekelweg 2, Delft, 2628CD, the Netherlands
[f] Marine Additive Manufacturing Centre of Excellence (MAMCE), University of New Brunswick, Fredericton, NB, E3B 5A1, Canada

ARTICLE INFO

Keywords:
Micromechanics
AlSi10Mg
Cast
Additive manufacturing
Eutectic silicon
Spheroidization

ABSTRACT

This study aims at assessing the effect of solution heat treatment (at a temperature just below the eutectic temperature) followed by various cooling rates on the microstructure and mechanical properties of additively manufactured AlSi10Mg and the cast counterpart. The mechanical properties were evaluated using a depth-sensing nanoindentation platform. The cast and additively manufactured parts were solutionized at 540 °C for 2 h followed by water quenching, air cooling, and furnace cooling. Results show extensive microstructural changes (e.g. size and morphology of eutectic-silicon phase) and evolutions in the mechanical properties of the heat-treated materials relative to the as-printed and as-cast ones. Besides, the microstructure and micromechanical properties of the materials broadly alter the cast and additive manufacturing conditions. Depending on the cooling condition, the mentioned cooling cycles directly affect the morphology of eutectic-silicon in both cast and additive manufactured materials starting with silicon fragmentation, then followed by silicon spheroidization, and silicon coarsening. The microstructural evolution affects the local micromechanical properties of the studied materials. The results of this study provide insights into the control of microstructure and hence mechanical properties of AlSi10Mg alloy by addressing suitable heat treatment cycles. This study, for the first time, assesses and compares the effect of various post-fabrication cooling rates in the cast and additive manufacturing conditions in an AlSi10Mg alloy.

1. Introduction

The Al–Si–Mg cast alloys, having low density combined with good mechanical properties, excellent castability, and heat-treatable capability, are particularly suitable for manufacturing large structural components as well as thin parts in a wide range of applications including the aerospace and automotive industries to a variety of engineering parts [1–4]. Among this alloy family, AlSi10Mg is a hypoeutectic alloy that can be additively manufactured due to its narrow solidification range which reduces the hot cracking susceptibility during cooling [5–7]. The main advantage of additively manufactured aluminum alloys, as compared with the cast counter material with dendritic microstructure, is superior mechanical and formability properties thanks to refined grain structure (due to very high solidification rate) [8]. When it comes to the additive manufacturing of aluminum alloys, and particularly AlSi10Mg as an alloy receiving the most attention, complex bulk, and open-cell structures with great strength ratio (strength-to-weight ratio) and acceptable formability can be manufactured. Besides, most of the cast AlSi10Mg alloys must be post-machined to achieve the desired surface finish and final dimensions; this extra processing would be eliminated, especially for hard-to-machine (or hard-to-deform) aluminum alloys when considering additive manufacturing as a fabrication direction. The main challenges of the laser-based powder additive manufacturing processes [8,9] in the fabrication of AlSi10Mg alloy are powder-related issues (e.g. high reflectivity, high thermal conductivity, and low laser absorptivity), process-induced defects (epitaxial growth of grains, porosity, lack of fusion, and

* Corresponding author.
E-mail address: meysam.haghshenas@utoledo.edu (M. Haghshenas).

https://doi.org/10.1016/j.rinma.2021.100178
Received in revised form 27 January 2021; Accepted 15 February 2021
Available online 2 March 2021

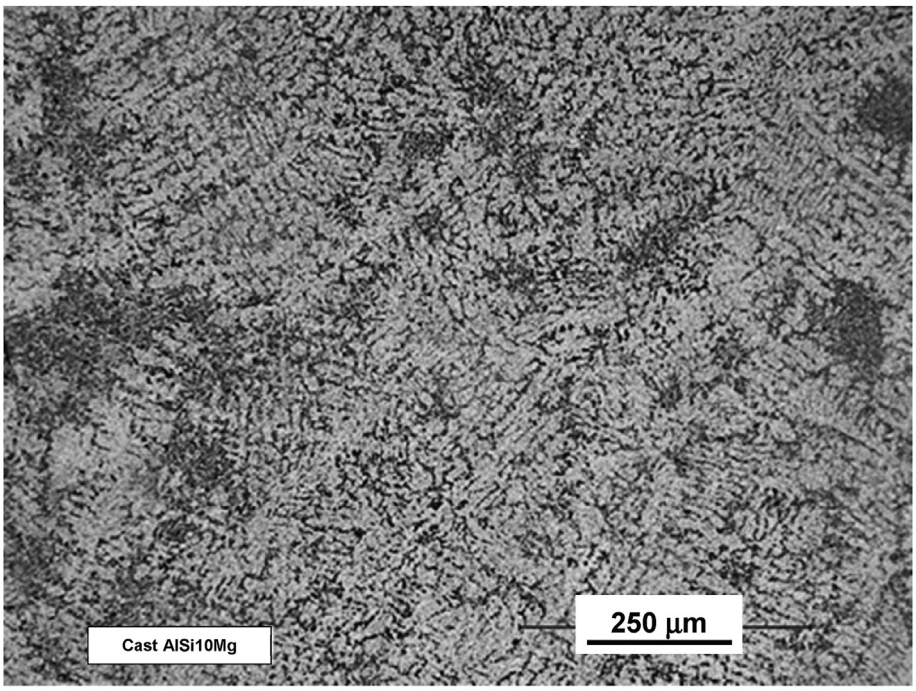

(a)

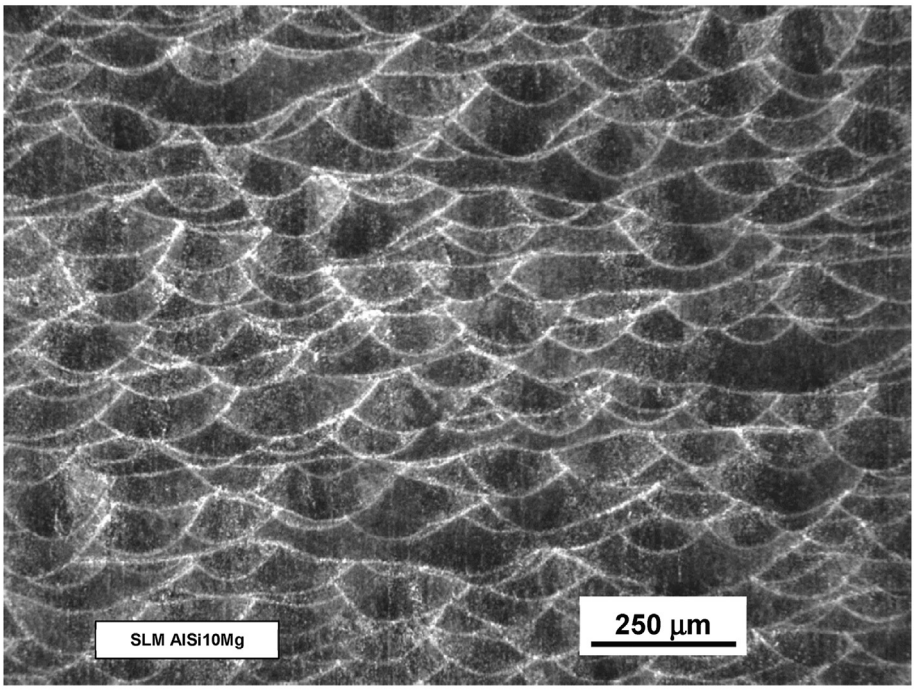

(b)

Fig. 1. Optical micrographs of (a) as-cast, (b) as-printed AlSi10Mg.

inclusions) and residual stress produced by the sharp thermal gradient of the laser-based additive manufacturing processes.

Among various metal additive manufacturing techniques, selective laser melting (SLM) has become a robust metal additive manufacturing method offering fast, reliable, and cost-effective production of complex, completely dense metal parts [10–12]. Also, conventional metal manufacturing processes (e.g., casting, forging) may not even be capable of producing parts in some cases, that can be produced using SLM [13]. The microstructure of the cast AlSi10Mg is noticeably different from the SLM parts [14]. The casting process greatly influences the microstructural features such as the morphology and size of eutectic silicon and intermetallic compounds (primary Mg_2Si particles and Fe-rich intermetallic phases) and thus plays a vital role in the mechanical properties of the alloy. Due to the slow cooling rate in the traditional AlSi10Mg casting processes, the solid solution of silicon in aluminum disintegrates and precipitates in a relatively coarser form. Along with dispersed primary α-Al, the aluminum matrix is surrounded by a continuous eutectic structure of Al and Si [12] where some intermetallic compounds also exist, and overall a dendritic microstructure is obtained. Ductility and strength, as well as machinability of the alloy, is

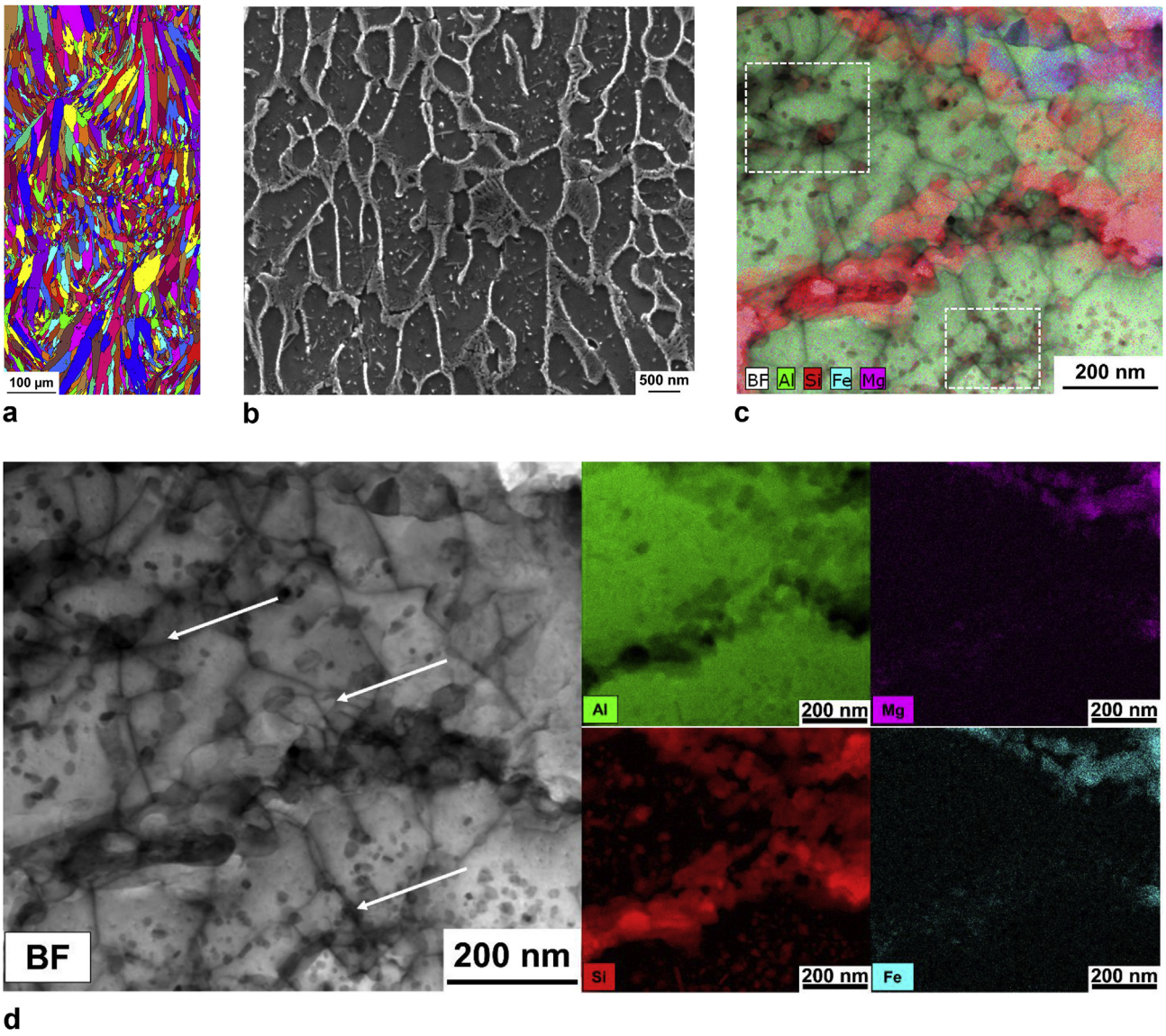

Fig. 2. (a) EBSD unique color grain map, (b) SEM micrograph, and (c) STEM-BF micrograph of SLM AlSi10Mg superimposed with the EDS elemental maps of Al, Si, Fe, and Mg, and (d) the individual element maps. Dashed squares in (c) show the entangled network of dislocations.

significantly affected by the eutectic Al + Si phase present in the microstructure [15–17].

On the other hand, due to repeated ultra-fast cooling and solidification throughout the SLM process, the additive manufactured (as-built) AlSi10Mg parts consist of a fine network of Si particles inside the aluminum matrix, and mechanical properties of the alloy get enhanced by the modification occurring in the eutectic silicon phase [2,18]. The ultrafine microstructure of SLM AlSi10Mg is characterized by cellular α-Al phase and fibrous Si particles and is responsible for higher hardness and tensile strength of the parts [19–23]. The fibrous Si network around the Al matrix is formed by the ejection of the Si particles during the high cooling rate (10^3–10^6 °C/s) of the SLM process [24,25]. The extremely fine microstructure and the consequent high volume of grain boundaries serve as main factors toward limiting the dislocation motion and, therefore, enhancing the mechanical performance of the AM parts [14, 20].

AlSi10Mg is a heat treatable alloy meaning that the heat treatment modifies the microstructure of the material; the most common heat treatment on AlSi10Mg is the T6 heat treatment consisting of solution treatment, quenching, and artificial aging. This is typically performed on AlSi10Mg alloys for desirable modification of microstructure and mechanical properties [26–29]. Modification of coarse and acicular Si phase (spheroidization), homogenization of the composition, and disintegration of dissolvable phases containing Mg or other trace elements are directed by solution heat treatment [30]. Quenching preserves the high temperature solutionized phase at ambient conditions and inhibits the precipitation. Aging uniforms the distribution of precipitates and other segregated solute atoms which results in the strengthening of the alloy [31]. Precipitation and coalescence of the Si particles occur during solution heat treatment which reduces the concentration of Si in the Al matrix and influences mechanical properties [32]. However, the cast and SLM AlSi10Mg follow two opposite trends (in terms of hardness) upon heat treatment. The T6 heat treatment increases the hardness of the components produced through casting whereas, for the AM components, the hardness value at as-built condition is not exceeded for any of the combinations of temperature and time applied [33,34]. In the case of SLM AlSi10Mg, aging the as-built material (without solution heat treatment) results in strength enhancement through the formation of more stable nanosized Si precipitates [35]. Such behavior is because of the extremely fine microstructure of the AM components, which implies a high density of grain boundaries, that inhibits the dislocation motion and results in higher material hardness [27]. After the treatment at high

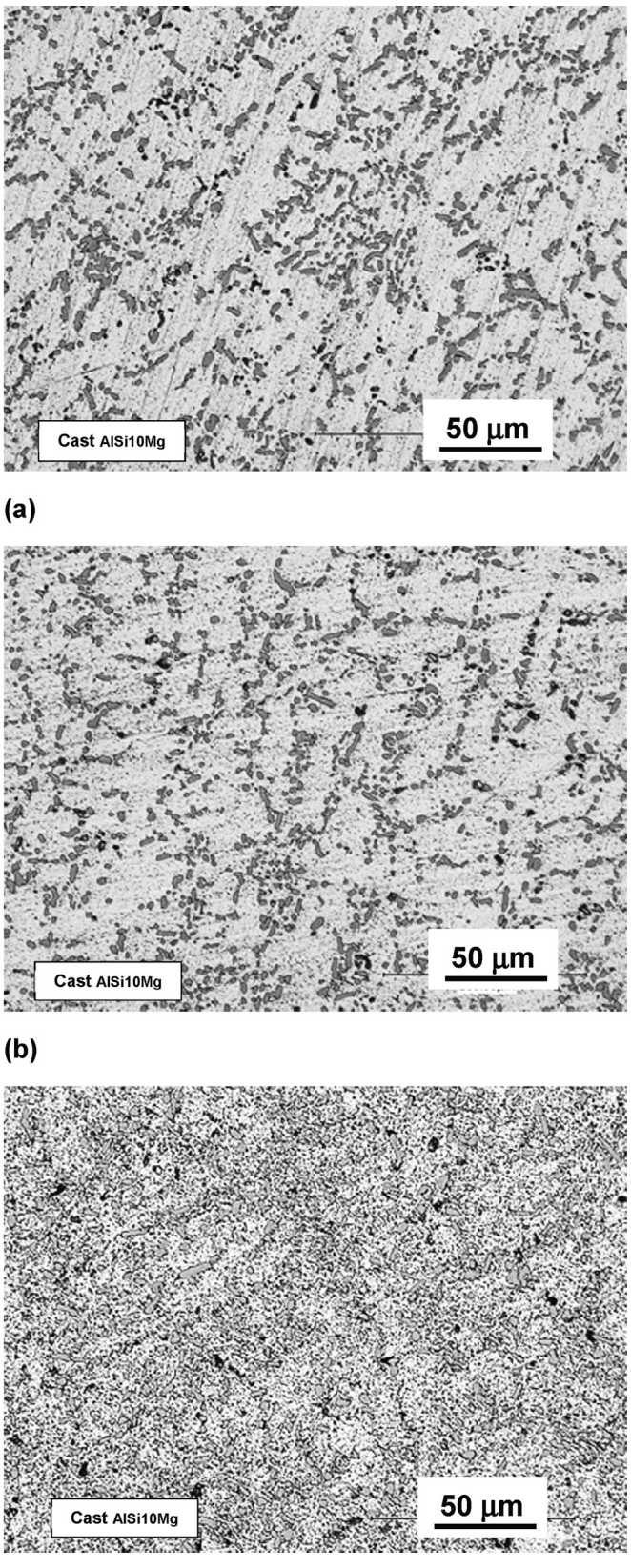

Fig. 3. Optical micrographs of various heat-treated cast AlSi10Mg, (a) water quenched (WQ); (b) air cooled (AC); (c) furnace cooled (FC).

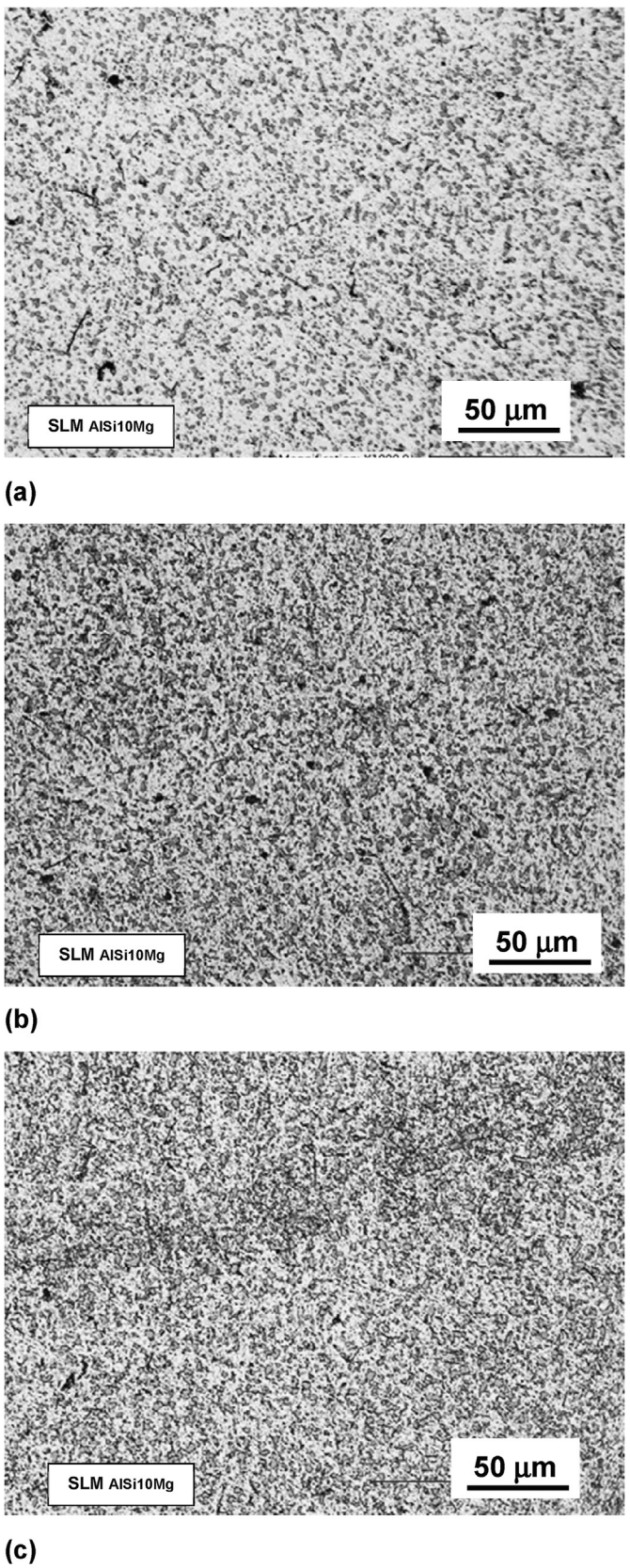

Fig. 4. Optical micrographs of various heat-treated SLM AlSi10Mg, (a) water quenched (WQ); (b) air cooled (AC); (c) furnace cooled (FC).

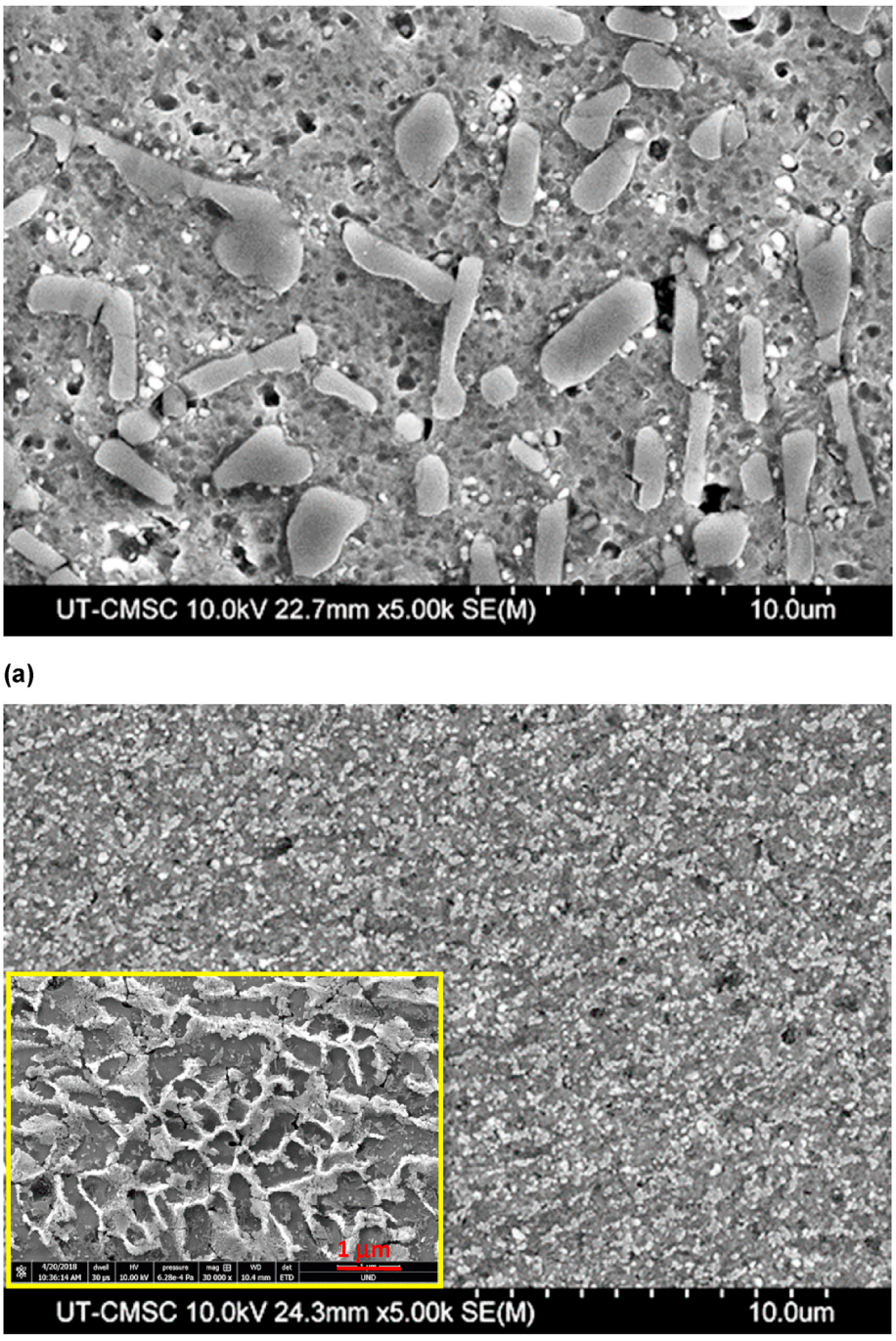

Fig. 5. The SEM micrographs of (a) cast AlSi10Mg, and (b) SLM AlSi10Mg with a fibrous network of silicon phase.

temperature, the fine-grained microstructure of AM components is lost and the Si particles get coarsened. Due to the coarsening of the microstructure at high temperatures, the number of grain boundaries decreases, and dislocation motion accelerates resulting in the drop in hardness values (for AM components) [27,33]. In the case of cast AlSi10Mg, diffusion of Si atom occurs during solutionizing and causes fragmentation and spheroidization of the particles of eutectic Si [36,37]. Because of the high thermal stability of the intermetallic phases (Mg_2Si and needle-like Fe-rich intermetallic phases) present in the microstructure of the cast alloy, solution treatment may not change such phases. But the size of those intermetallic particles becomes smaller upon T6 treatment [38]. While in the case of their SLM counterpart, these particles go through coarsening and reach a diameter of some micrometers [22]. Also, the eutectic Si network structure developed along the α-Al cell is broken, which leads to the opposite trend in terms of hardness of cast and SLM AlSi10Mg. However, the precipitation and coalescence of the Si particles can be controlled toward obtaining the desired mechanical properties by adopting a specific heat treatment for exploiting the potentialities of this alloy at best.

Although both cast and SLM AlSi10Mg are extensively studied materials, most of the published studies are focused on conventional heat treatment and macro-scale mechanical testing. Moreover, there is no such study that involves comparison and investigation of microstructure and small-scale mechanical properties of as-cast, as-built, and heat-

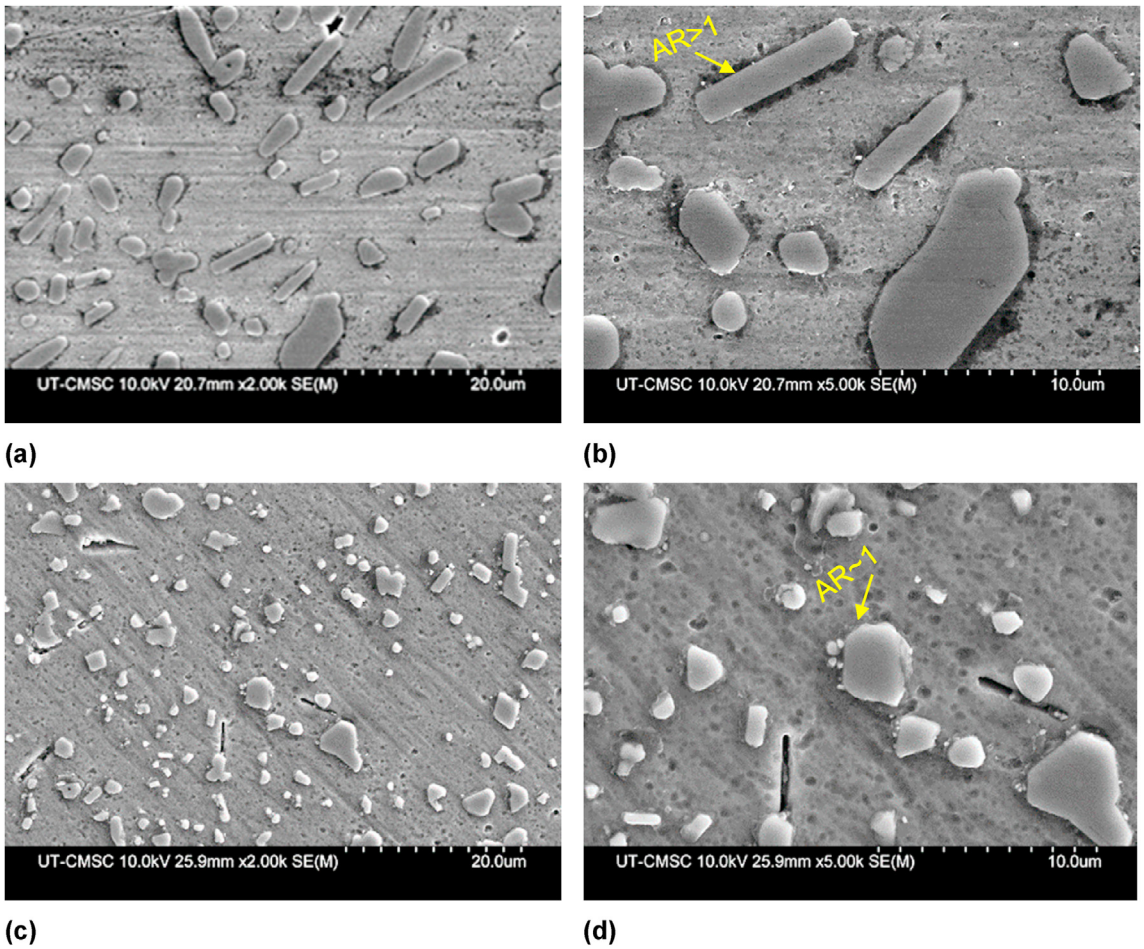

Fig. 6. The SEM micrographs of water quenched (WQ) samples, cast (a, b) and SLM (c, d), at two different magnifications. As seen, most of the eutectic Si networks are broken into fine Si particles that are dispersed more uniformly in the Al matrix. The yellow arrows show the aspect ratios (AR) for a rod-like Si and a spheroidized Si particle.

treated counter samples. The objectives of the study are to assess and compare the effect of various heat treatments (solutionizing followed by cooling at different quenching media) on the microstructure and micro-mechanical properties of cast and SLM AlSi10Mg. In doing that, morphology and distribution of eutectic Si within the microstructure of as-cast, as-built, and heat-treated counter samples were assessed employing optical and scanning electron microscopy. Small-scale mechanical properties were evaluated employing the depth-sensing nano-indentation technique. This study involved solution heat treatment on both cast and SLM AlSi10 Mg at 540 °C for 2 h followed by water quenching, air cooling, and furnace cooling. This heat treatment allowed us to track the microstructure and mechanical property evolution from an extremely high cooling rate to a low cooling rate. This is extremely important as microstructural features such as morphology, size, and distribution of eutectic Si and intermetallic particles are significantly influenced by cooling rates which ultimately make changes in mechanical property. Small-scale mechanical property assessment and comparison of the as-built and heat-treated cast and SLM samples at various cooling rates made this study unique and a thorough analysis of AlSi10Mg alloy.

The results presented in this work can be used for comprehensive assessments on the correlation between microstructural states of non-equilibrium alloy conditions and their mechanical performance in future work. With a detailed understating of microstructural changes upon cooling at various media, proper heat treatment parameters can be derived to control the microstructure (and mechanical properties) and thus produce well-controlled material conditions. A comparison of these states between SLM and cast conditions will allow the investigation of the mechanical strength of the as-fabricated microstructure and cooling-induced precipitates with different morphologies. Accordingly, evidence of vigorous strengthening mechanisms can be obtained to improve plasticity models.

2. Experimental procedure

The cast and additive manufactured (SLM) AlSi10Mg samples were provided by Goodfellow USA and Carpenter Additive, respectively. The samples were firstly solutionized at 540 °C for 2 h in a bubbling fluidized bed containing alumina particles (Techne FB-08 Series Precision Fluidized Bath) where temperature stability and uniformity for heat treatment are well controlled. This is then followed by cooling at different media including water (water quenched, WQ), air (air-cooled, AC), and furnace (furnace cooled, FC). To reveal the microstructure, the samples were prepared through a standard metallography procedure (including mechanical grinding and polishing) and etched in a Keller's reagent (2.5% HNO_3, 1.5% HCl, 1.0% HF, 95.0% distilled water).

The SLM AlSi10Mg sample was studied using electron backscatter diffraction (EBSD) and transmission electron microscopy (TEM) to analyze the details of the microstructure at different length scales. The details of sample preparation and analyses have been reported in Ref. [39]. EBSD measurements were performed in a high-resolution field emission gun scanning electron microscope (FEG-SEM) (of type FEI QUANTA™ 450) on a 1000 × 1000 μm^2 region with a step size of 1 μm to obtain the local crystallographic orientations. The diffraction patterns

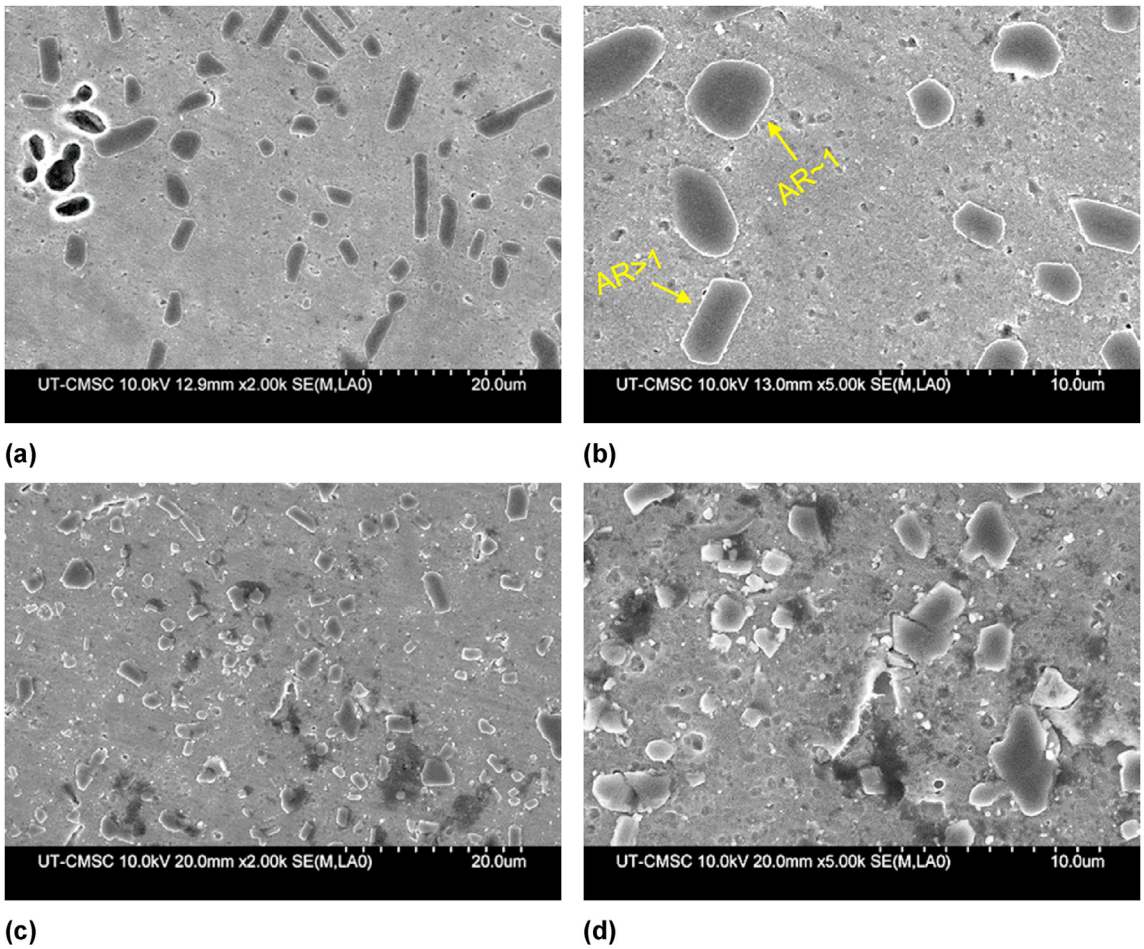

Fig. 7. The SEM micrographs of air-cooled (AC) samples, cast (a–b) and SLM (c–d), at two different magnifications.

were collected using the TSL® OIM data collection software and were post-processed using the OIM data analysis software. The crystallographic textures were calculated by the harmonic series expansion method with a truncation of L = 16 and a Gaussian-Half-Width of 5°.

An FEI Tecnai Osiris TEM equipped with a 200 keV X-FEG gun was used to conduct the TEM analyses. The Super-EDS X-ray detection system combined with the high current density electron beam in the scanning mode (STEM) was also utilized to analyze the precipitates. Spatial resolutions in the order of 1 nm were obtained during EDS elemental mapping by using a sub-nanometer electron probe.

To extract the small-scale mechanical properties of the as-built (cast and additively manufactured) and heat-treated sample, an instrumented indentation platform, an iMicro nanoindenter (KLA), equipped with a self-similar pyramidal diamond Berkovich indenter (tip radius 100 nm) was used. The instrumented indentation is considered a semi-destructive testing method and offers a fast, precise, and robust procedure to determine the local mechanical properties of materials [40]. In this study, constant load indentation experiments were performed with a peak load of 400 mN, a load rate of 10 mN/s, and a dwell time of 2 s. Corresponding indentation hardness, young's modulus, and load-depth data for each sample were extracted from the system and analyzed employing the Oliver-Pharr method [41]. Optical and scanning electron microscopy was carried out using a Keyence VHX-600 Digital Microscope and a Hitachi S-4800 UHR Scanning Electron Microscope (SEM), respectively, to link the evolution in microstructural features with the differences in mechanical properties.

3. Results

3.1. Microstructural observations

Fig. 1 presents the optical microstructure of cast and SLM AlSi10Mg alloy, respectively. The two considered processes (casting and SLM) lead to completely different microstructures and this is due to drastically different cooling rates and solidification conditions governing each process. In the case of the as-cast alloy, a dendritic structure is revealed in Fig. 1a. The α-Al phase surrounded by the acicular eutectic Si particles mainly featured the microstructure in the as-cast condition. For the SLM counterpart, the microstructure consists of overlapped melt pools (Fig. 1b), which is due to the progressive laser rastering which causes melting and solidification of successive layers of materials. Inside the melt pools, a very fine dendritic structure of the α-Al matrix bounded by the eutectic Si phase developed. The dendrites possess a columnar structure due to the unidirectional heat transfer during the solidification. These dendrites mainly developed in the building direction. The fast cooling rates during the SLM process resulted in the development of a very fine structure and a substantial difference between the cast and SLM microstructures. An important characteristic of SLM AlSi10Mg is the evolution of a hierarchical microstructure in this material due to the unique solidification conditions that occurred in the SLM process [39]. In a hierarchical microstructure, different features exist at different length scales. To better analyze these features, in addition to optical microscopy, the finer details of the microstructure were studied using SEM and EBSD on a micro-scale, and TEM in a nanoscale. Fig. 2a is the EBSD unique color grain map of the SLM AlSi10Mg, where columnar grains developed along the building direction are observed. The grains possess the same

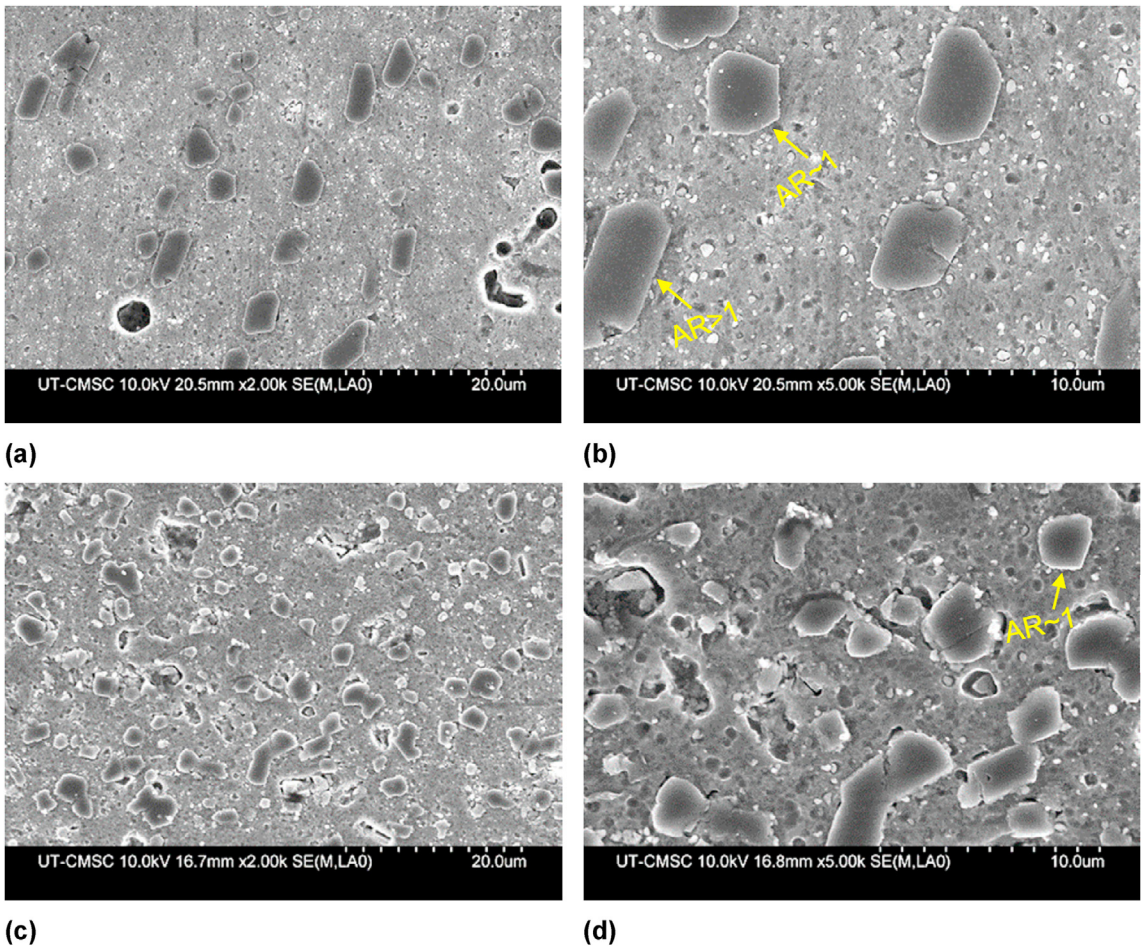

Fig. 8. The SEM micrographs of furnace cooled (FC) samples, cast (a–b) and SLM (c–d), at two different magnifications.

columnar morphology as the dendrites, however, their size is at least one order of magnitude larger than the dendritic structure, as shown in Fig. 2b. The nano-scaled details of the microstructure inside a melt pool are presented in Fig. 2c, where Si precipitates are dispersed in the matrix. Fig. 2d shows the individual elemental maps. Moreover, an entangled network of dislocations developed in the matrix is observed (see dashed boxes in Fig. 2c). These dislocations interact with both the Si precipitates and the eutectic Si in the melt boundaries. These microstructural features enhance the strength of the SLM AlSi10Mg material through Hall-Petch, Orowan, and dislocation hardening mechanisms [39,42].

Figs. 3 and 4 show the microstructure of heat-treated cast and SLM AlSi10Mg alloys, respectively. The heat treatment process homogenized the as-cast structure, changed the morphology of eutectic silicon, and dissolved intermetallic phases within the matrix. For the cast alloy, the distribution of Si particles in the aluminum matrix is non-uniform and the acicular eutectic Si particles disintegrated and rounded upon solutionizing at 540 °C (Fig. 3a–c) through the Ostwald ripening mechanism [43]. In the present study, Ostwald ripening is indeed due to a solid-state diffusional growth of the eutectic-Si particles which is a thermodynamically driven spontaneous process. That is, smaller particles are less energetically stable than the larger particles and this is because the well-packed (ordered) internal atoms are more stable than the surface atoms. A lower energy state is achieved when large particles, with their lower surface to volume ratio and therefore lower surface energy associated with the interface between the silicon particles and the Al matrix, are present within the structure. Therefore, atoms on the surface of small particles tend to detach and diffuse toward the surface of larger particles. Therefore, the number of smaller particles continues to shrink, while larger particles continue to grow.

For the SLM counterparts, the heat treatment process resulted in a more uniform distribution of Si particles in the aluminum matrix (Fig. 4a–c). Fig. 5 clearly shows the differences in the as-cast and as-built AlSi10Mg microstructures. The size of the eutectic-silicon is tangibly coarser in the cast material as compared with the SLM counterpart. Besides, the SLM alloys consist of a cell structure as seen in the high magnification inset in Fig. 5b. The solidified melt pools of the as-built sample show a fish scale pattern (see Fig. 1b) that is inherent to the high solidification rate of the SLM process. The solidification rate and the thermal gradient are the two main parameters in defining cellular structure associated with most SLM processes [44]. In other words, the very fine cellular microstructure is due to the high thermal gradients and cooling rates of the SLM process. The cellular network consists of fibrous eutectic Al/Si along the cell boundaries of the supersaturated Al solid solution matrix. It is worth noting that in the SLM process, due to very high heat flow along the Z-orientation, the solidification of the columnar cells occurs in the Z-direction. For AlSi10Mg ally, with a face-centered cubic (FCC) crystalline structure, the FCC crystals prefer to grow in the <100> direction [45].

Figs. 6–8 show the SEM micrographs of the cast and the SLM materials that are all solutionized at 540 °C for 2 h, then cooled at different rates (e.g. using different cooling media). Solutionizing the cast AlSi10Mg resulted in substantial growth of the Si particles as a result of Si diffusion and particle coalescence (Ostwald ripening). Moreover, the cooling condition affected the morphology of Si precipitates. While the WQ sample consists of mainly acicular Si particles, more sphericity of the Si precipitates was achieved in the AC and FC samples. Such a change in the morphology is due to the longer exposure time to high temperatures which led to the reduction in surface/volume ratio. On the other hand,

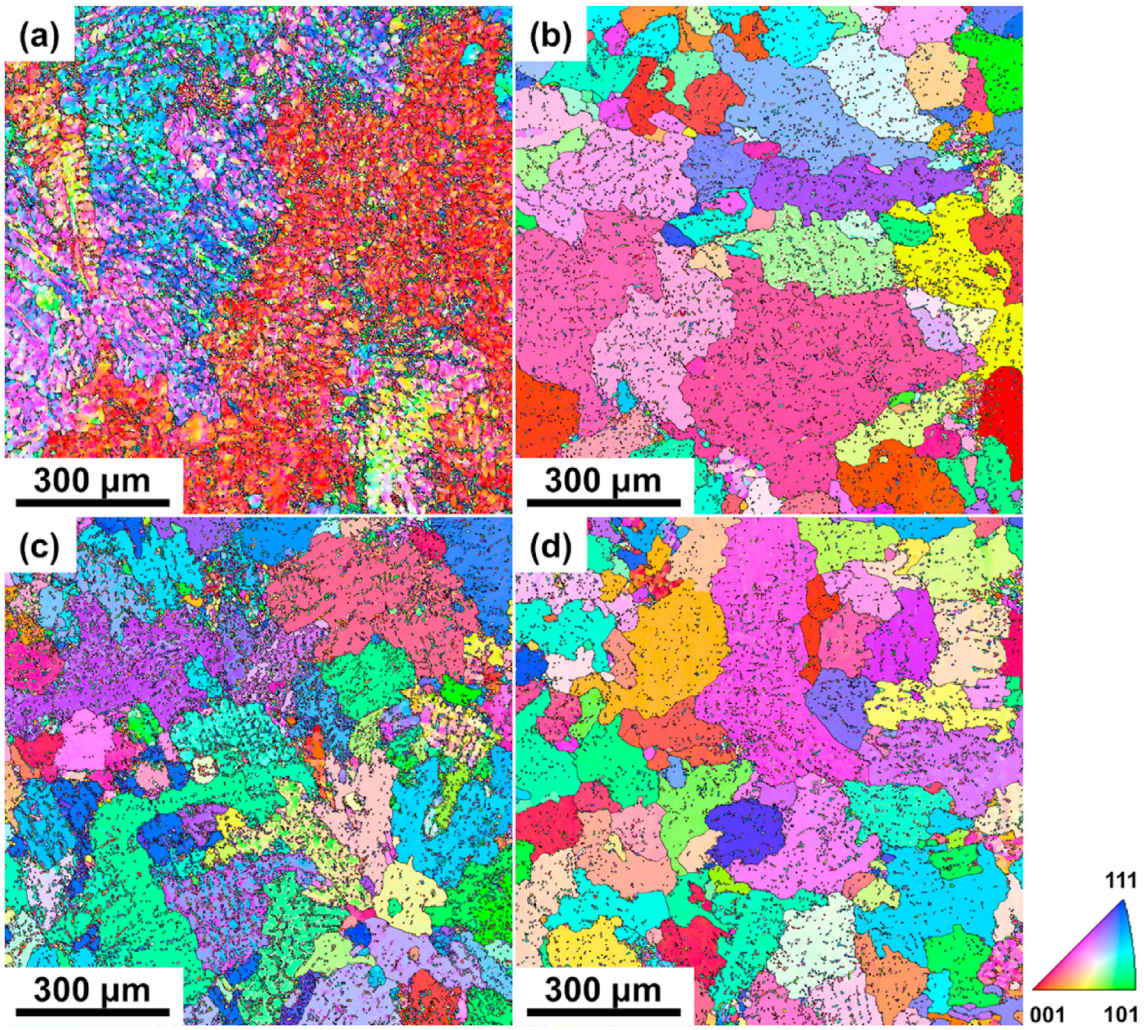

Fig. 9. EBSD IPF maps of cast AlSi10Mg materials; (a) as-cast, (b) WQ, (c) AC, and (d) FC.

the structure of the Si precipitates, and eutectic Si walls significantly changed in the SLM AlSi10Mg after heat treatment. The eutectic Si walls completely vanished and dispersed Si precipitates evolved in the microstructure. By changing the cooling condition from WQ to FC, the Si particles coarsened. Nevertheless, the size of the Si particles in the cast AlSi10Mg is larger than that in the SLM AlSi10Mg after identical heat treatment cycles.

Something that can be noticed from Figs. 6–8 is the changes in the aspect ratio (AR), the ratio of major axis length to minor axis length [46], of the eutectic silicon particles upon solution treatment followed by cooling at different media. We assume the AR of a sphere and a rod-like fiber to be 1 and > 1, respectively. The transformation from a fibrous-like Si particle to near-spherical Si particle results in an aspect ratio close to 1 (see the yellow arrows in Figs. 6–8). That is, the aspect ratio distribution of the eutectic-Si particles is further crooked to smaller values representative of near-equiaxed Si spheres. This is due to the loss of the interconnection of the eutectic phases followed by spheroidization of the disintegrated rod-like Si particles.

Further analysis of the effect of heat treatment on the microstructure of the samples, specifically the grain structure and microtexture, was conducted using EBSD. The EBSD IPF maps of the cast and SLM samples in the as-fabricated and heat-treated conditions are shown in Figs. 9 and 10. The IPF maps have been superimposed with the grain boundary (GB) maps. The as-cast AlSi10Mg represents a typical dendritic structure, where both the primary and secondary dendrite arms are visible as high angle grain boundaries. However, the microtexture does not alter between the secondary arms inside a dendrite, referring to the IPF map. Heat treatment of the cast AlSi10Mg, regardless of the cooling condition, resulted in the dissolution of the secondary dendrite arms and evolution of an equiaxed grain structure. In the heat-treated cast AlSi10Mg samples, a large grain structure with a random texture is observed. The grain structure and microtexture of SLM AlSi10Mg (Fig. 10) are different from those of the cast counterpart since the rapid and directional solidification resulted in the evolution of fine columnar grains, developed along the building direction. Some fine equiaxed grains are mainly developed over the melt pool boundaries due to partial remelting of the solid substrate. Referring to the EBSD IPF and GB maps, the heat treatment did not alter the microstructure and texture of the SLM AlSi10Mg material. The texture of SLM AlSi10Mg was further analyzed by developing the (001) pole figures (since (001) is the easy growth direction in the FCC metals) and the results are shown in Fig. 11. The common <001>//z (z: building direction) is observed in the SLM AlSi10Mg material, where the heat treatment did not have a significant effect on it.

3.2. Micromechanical characterization

To assess the small-scale properties, indentation experiments with five repeats are conducted on each material condition and average values are reported. Fig. 12 shows the representative indentation load (P) versus indentation depth (h) curves for as-fabricated (cast and SLM) and heat-treated AlSi10Mg materials obtained under a constant load of 400 mN. For the cast materials, Fig. 12a, the indentation depth is the least for the

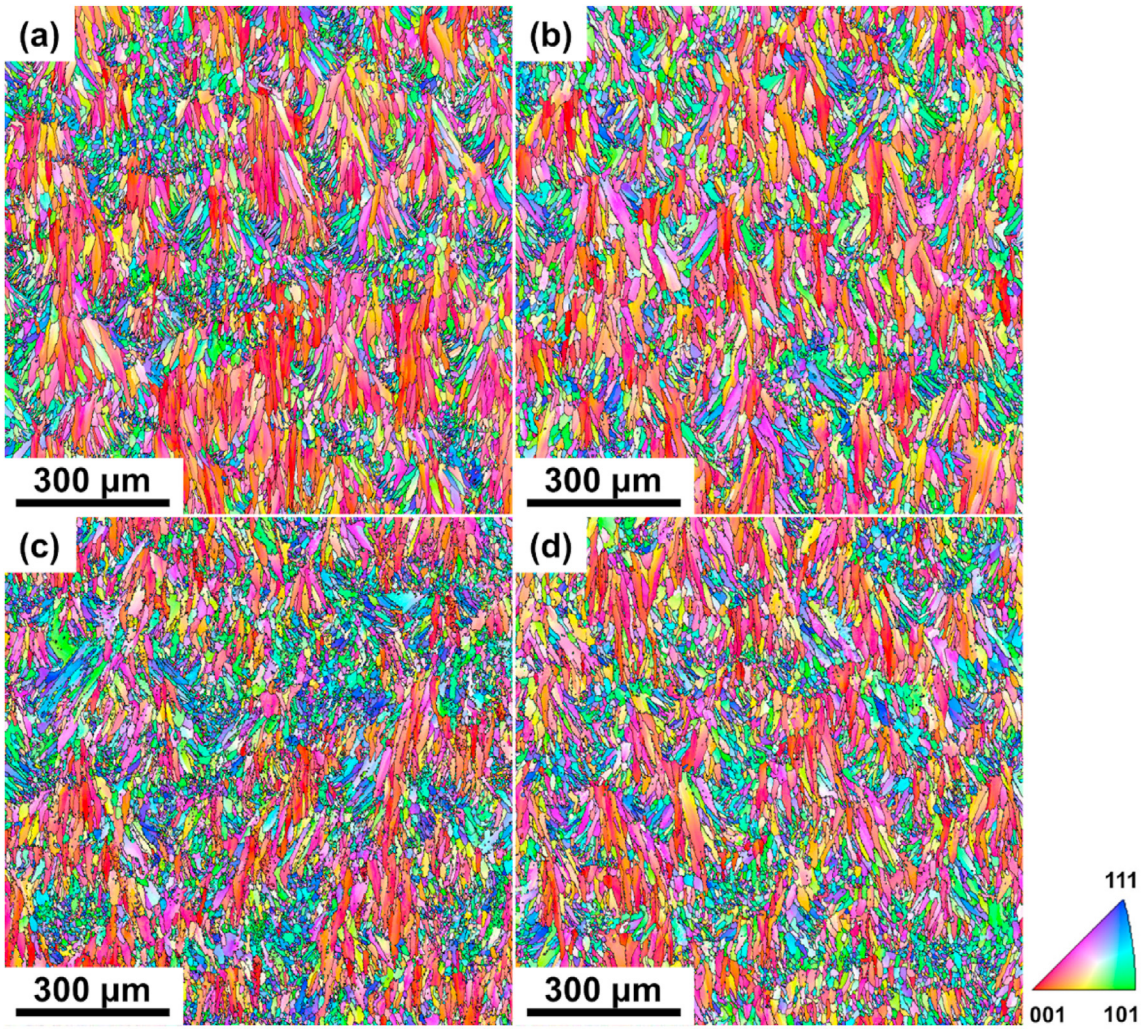

Fig. 10. EBSD IPF maps of SLM AlSi10Mg materials; (a) as-built, (b) WQ, (c) AC, and (d) FC.

water quenched sample and the as-cast structure shows the second-least depth. This shows that, among the cast samples, the WQ and the FC ones are the hardest and softest materials, respectively. The main reasons behind such a trend are extensively discussed in section 4.2 of the present paper.

For the SLM material, Fig. 12b, under a constant load, indentation depth for the as-printed sample is the least while upon heat treatment (solutionizing and cooling with different rates), indentation depth increases with a decrease in the cooling rate, confirming that the materials become softer. WQ sample (among cast materials) and as-built sample (among the SLM materials) are the ones with the highest strength (hardness). Among three different heat-treatments, furnace cooling involved the slowest cooling and resulted in the highest depth of penetration (h) in both cast and SLM samples. This means that the materials are in the softest state when cooled inside the furnace with a very low cooling rate. Besides, under a constant load, the overall indentation depth in the cast samples (as cast and FC states) is higher than the SLM materials in the same state. This is further depicted in Fig. 13a in terms of hardness which shows that the as-built material is harder than the as-cast counter material which is attributed to the fine cellular structure of the SLM material. However, post-solutionizing cooling at various rates significantly altered the strength of the materials; i.e. for the WQ and AC states, the strength of cast materials significantly improved and exceeded the SLM counter materials. Considering the standard deviation, the differences of reduced modulus values for the SLM samples and the cast materials are not very sharp though the modulus of the SLM materials is higher than that of the cast samples and follows a relatively constant trend with different heat treatment cycles.

Employing a self-similar pyramidal (Berkovich) indenter, the indentation hardness (stress) can be calculated from Eq. (1) [47–49]:

$$\sigma_{ind} = \frac{P}{24.5(h + 0.06R)^2} \tag{1}$$

where P is the indentation load (mN), h is indentation depth (nm), and R is the indenter tip radius (100 nm for the indenter used in this study). Fig. 14 shows the indentation stress versus indentation depth for the cast and the SLM materials in the as-fabricated and heat-treated conditions. A clear indentation size effect (ISE), an increase in the indentation stress with a decrease in the indentation depth, is observed.

The elastic-plastic quantitative analyses were performed on the data produced by the nanoindentation system. The plasticity index (ψ) provides insights into the elastic and the non-elastic (either plastic or viscoelastic) response of a material. The Ψ describes the relative plastic/elastic behavior of the material effectively when it undergoes external stresses [50,51]:

$$Plasticity\ Index,\ \psi = \frac{A_1 - A_2}{A_1} \tag{2}$$

where A_1 is the area under the loading section and A_2 is the area under the unloading section of the load-displacement curve. The irreversible or plastic work during the nanoindentation test is indicated by the

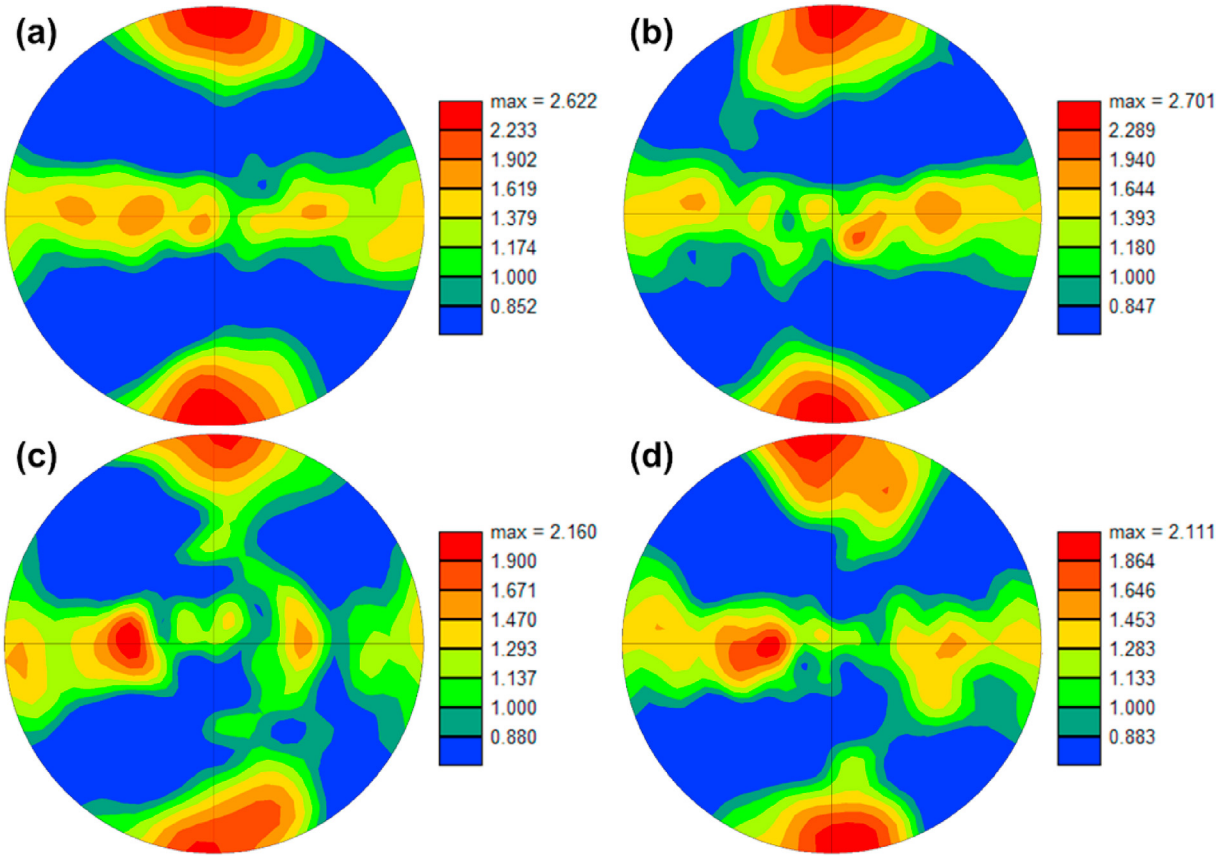

Fig. 11. (001) EBSD pole figures of SLM AlSi10Mg materials; (a) as-built, (b) WQ, (c) AC, and (d) FC.

difference between A_1 and A_2. The value of plasticity index (ψ) should be between 0 and 1, where fully elastic behavior of the material is characterized by $\psi = 0$, fully plastic behavior is characterized by $\psi = 1$, and elastic-plastic response is considered when $0 < \psi < 1$. In this study, all the nanoindentation tests were performed using the same indenter and the plasticity index can be written as:

$$\psi = \frac{h_m - h_e}{h_m} = \frac{h_r}{h_m} \tag{3}$$

where h_m is the maximum indentation depth and h_e is the elastic reversible indentation depth which is obtained from the load-displacement curve recorded during the nanoindentation test. The residual depth in the nanoindentation test is indicated by the difference between h_m and h_e.

Fig. 15 presents the changes in the value of the plasticity index (ψ) in the as-fabricated (as-cast & as-built) and heat-treated AlSi10Mg alloys. The highest values of the plasticity index (ψ) are found at the FC condition for both cast and SLM samples. A higher value of plasticity index (ψ) indicates that the plastic work done during the nanoindentation is the largest for the FC condition where plastic deformation imposed by the indenter can happen to a larger extent since the material is softer in the FC state.

Indentation hardness and reduced modulus can be used as proximity for the wear resistance based on Eq. (4) [52,53]. Fig. 16 presents the changes in wear resistance index (WRI) of the cast and SLM AlSi10Mg upon heat treatment which is determined using Eq. (4).

$$WRI = \frac{H^3}{E_r^2} \tag{4}$$

As seen in Eq. (4) there is a direct relationship between the WRI and the indentation hardness. The FC state indicates the least WRI since it is the softest structure among others.

4. Discussion

For the AlSi10Mg alloys produced by casting and/or additive manufacturing, thermal treatment is an important post-fabrication step as it can be used to tailor mechanical properties and microstructure properly. For instance, a common heat treatment in cast Al–Si alloys is solution treatment, at a temperature just below the eutectic temperature for long enough to allow solutionizing of the second phases and alloying constituents, followed by quenching, to maintain a homogeneous supersaturated structure at ambient temperature, and artificial aging at intermediate temperatures. This heat treatment cycle results in the formation of precipitates in the matrix which affects the mechanical strength of the alloy. The objective of this paper is not to assess the aging of the cast and SLM AlSi10Mg but to discuss the effect of various cooling rates after solutionizing, soaking for 2 h at 540 °C, in different media (water, air, furnace) on microstructure evolutions and micromechanical characterizations of the alloys.

4.1. Microstructural characterization

Upon proper solutionizing, the alloy constituents and second phase particles would be dissolved in the aluminum matrix as much as possible while the size and morphology of rod-like eutectic-Si would change. The latter includes fragmentation or dissolution of the eutectic silicon branches and spheroidization of the separated branches. This morphological transformation of the eutectic silicon is a consequence of the surface and bulk diffusion of Mg and Si elements into the matrix [54]. Because of the interface defects between eutectic Si and aluminum matrix (e.g. necking, sharp tips, and corners of eutectic-silicon fibers), the required chemical potential gradient is formed to induce the surface

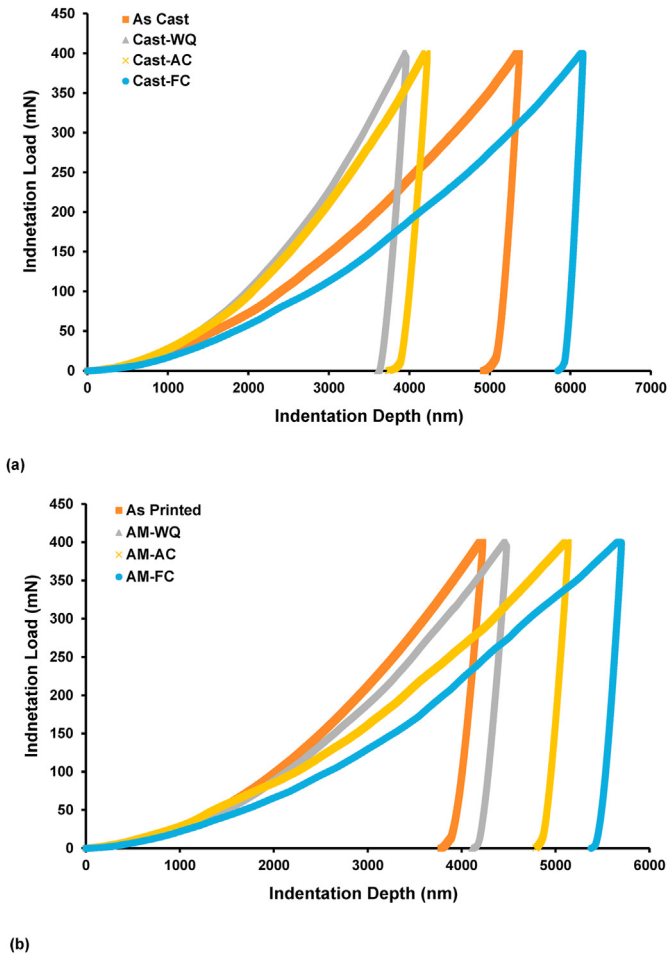

Fig. 12. Representative load-depth curves (a) cast, (b) SLM AlSi10Mg.

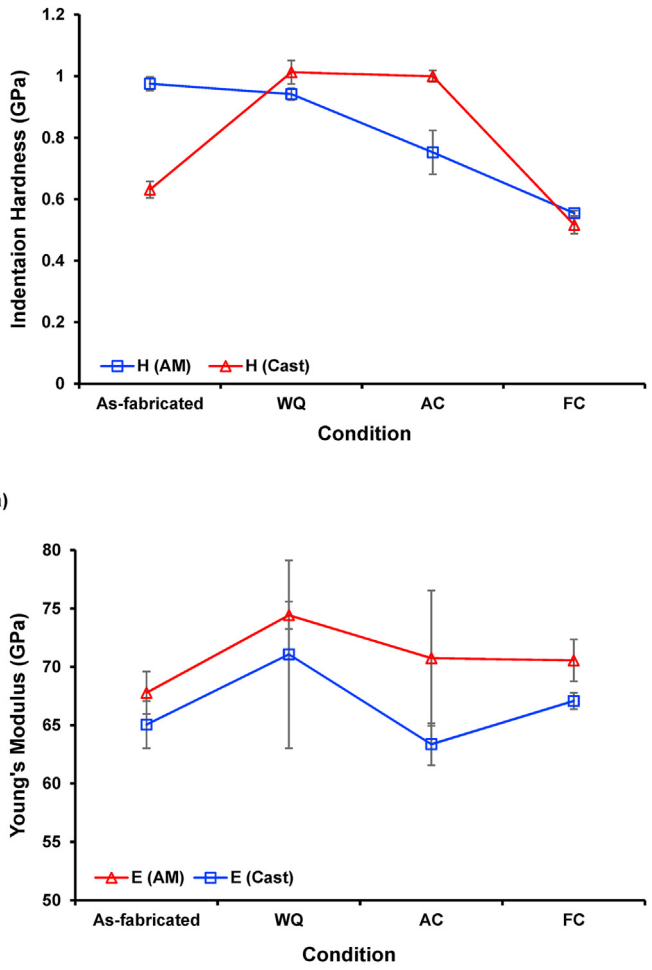

Fig. 13. Evolution of indentation hardness (a) and reduced modulus (b) for the cast and SLM conditions.

diffusion. Therefore, the coarse eutectic silicon fibers separate into smaller segments (fragmentation), and then spheroidize and coarsen. The spheroidization of the fragmented Si particles is thermodynamically spontaneous as the systems strive to reduce the surface energy under the synthetic effects of surface curvature and temperature. When enough time and temperature are provided to the system, based on Ostwald ripening, many Si atoms diffuse and adhere to the surface of larger particles therefore small Si particles eventually disappear while large Si particles further coarsen. According to the literature, solutionizing at 540 °C for 2 h provides the optimum condition for the spheroidization of Si particles [54]. It is worth mentioning that the course Si particles are not necessarily spherical but exhibits facet characteristics and this is because of the preferred growth orientation of Si particles, <112> direction on {111} planes [55].

Based on Figs. 6–8, the Si-particles in the heat-treated SLM materials are finer and further spheroidized compared with the heat-treated cast counter materials. This is closely associated with the solidification cooling rate and therefore the starting microstructure of the cast and SLM materials. The high solidification rate, as what occurs in SLM AlSi10Mg material, can accelerate the spheroidization of eutectic Si particles during the subsequent solution treatment [56]. That is, in the SLM conditions, due to the higher cooling rate, the dendritic size is finer and subsequently, the diffusion distance is shorter. This results in the fragmentation (disintegration) stage of the eutectic-Si being shorter. Besides, the driving force for diffusion of Si is larger and this is due to the supersaturated condition for the high-cooling (solidification) rate of the SLM materials during the manufacturing process.

With a decrease in the cooling rate (i.e. AC and FC), since the materials remain at high temperatures (non-ambient) for a longer time, the driving force will be provided for grains and eutectic silicon to grow further. On the eutectic silicon, the particles would spheroid and coarsen. The coarsening is more pronounced for the cast AlSi10Mg microstructures as compared with the SLM counterparts. This is because the starting size of the eutectic silicon particles in the solutionized cast alloy is already coarser than the SLM alloy due to the slower solidification rate inherited in the casting process.

4.2. Micromechanical characterization

As observed in Figs. 12 and 13, the SLM AlSi10Mg shows higher average hardness values when compared with the cast counterpart. This agrees with other hardness trends reported by Kempen et al. [57], Zou et al. [58], and Padovano et al. [59] on the cast and SLM AlSi10Mg alloys. The overall strength of the cast AlSi10Mg alloy is mainly contributed to the intrinsic strength of pure aluminum and eutectic silicon particles [60]. However, the higher hardness (strength) of the as-built AlSi10Mg material, relative to the cast material, can be contributed to a rapid solidification rate, due to a very small melt pool as compared to the significantly large substrate beneath, which results in grain refinement, the formation of a silicon-rich cell structure, and the supersaturated solid solution of silicon in α-Al (i.e. 8.89 at.%) [61–63]. The solid solution strengthening is mainly because of differences in atomic radii of silicon (0.118 nm) and aluminum (0.143 nm) which create a strain field in the

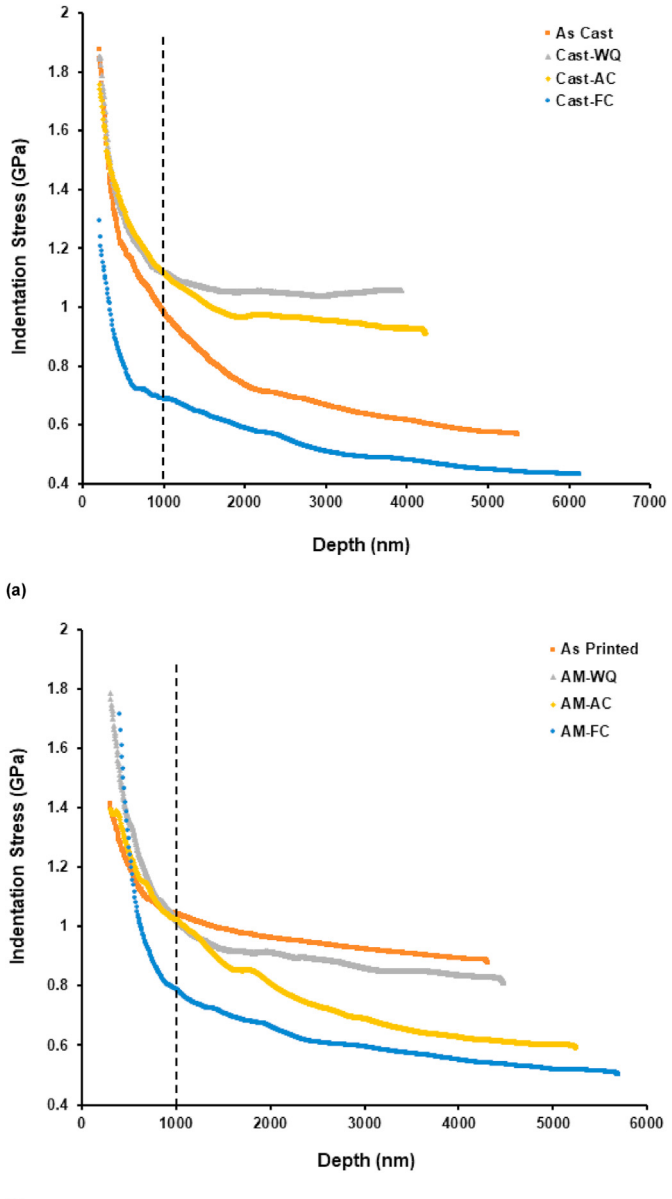

Fig. 14. Indentation size effect (ISE) of (a) cast, (b) SLM AlSi10Mg alloy.

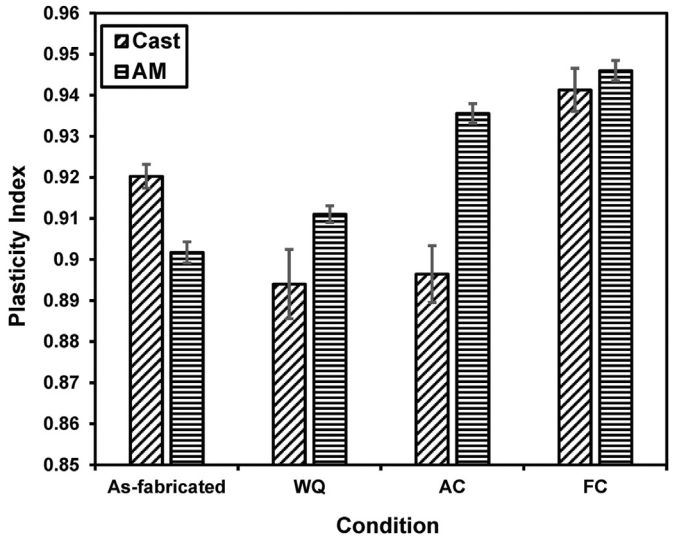

Fig. 15. Plasticity index for cast and SLM AlSi10Mg materials.

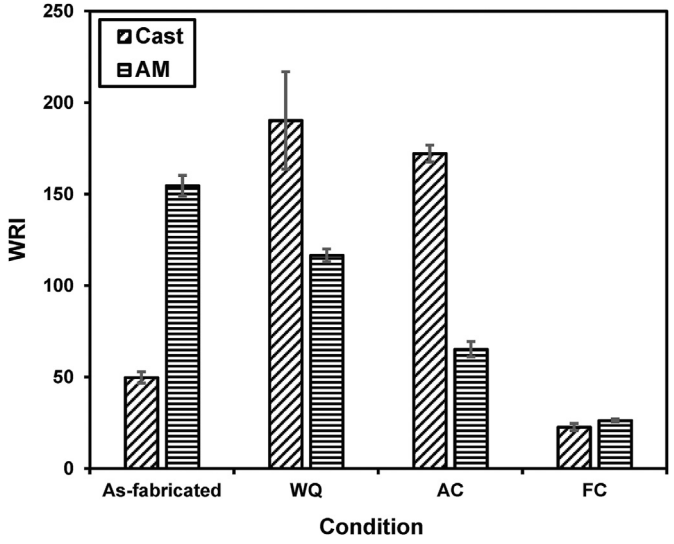

Fig. 16. Wear resistance for cast and SLM AlSi10Mg materials.

crystalline structure of the alloy acting as efficient obstacles against the dislocation motion. Besides, moving dislocations would be pinned by the Si precipitates and eutectic Si phases at cell boundaries via Orowan looping, and Hall-Petch mechanisms, respectively [25]. Mg clusters and Mg–Si co-clusters, which accelerate the precipitation of Mg_2Si, have been reported to provide excessive strengthening in the as-built AlSi10Mg alloy. Another source of hardening is the dislocation networks which strengthen the material through dislocation hardening. Considering the mentioned mechanisms, the as-built structure with no post heat treatment provides the hardest state of the printed AlSi10Mg alloy.

Upon a solutionizing thermal treatment, time and temperature are provided for (*i*) grains to grow, (*ii*) cell structure to progressively disintegrate, (*iii*) excessive dissolved Si to precipitate out, and weaken the solid solution strengthening, (*iv*) eutectic silicon to fragment, spheroidize, and coarsen, (*v*) and the annihilation of the dislocations. These parameters directly (and significantly) reduce the mechanical properties (e.g. hardness) of the AlSi10Mg alloy upon any post-fabrication heat treatment. That is why, the hardness values of the WQ, AC, and FC are lower than the as-built material.

According to Colley et al. [64], the dissolution of Mg_2Si particles occurs rapidly at solution temperatures and is completed within minutes. Upon rapid cooling (e.g. water quenching), since there is no time (driving force) for the dissolved particles and other alloying elements to precipitate out from the aluminum matrix, an unstable supersaturated solid solution of solute atoms and vacancies is formed. Indeed, the objectives of quenching are (i) to suppress precipitation during quenching to retain the maximum amount of the precipitation hardening elements in solution, (ii) to form a supersaturated solid solution at ambient temperatures, and (iii) to trap as many vacancies as possible within the atomic lattice [65,66]. The supersaturated solid solution structure is unstable therefore upon any post mechanical work (i.e. nanoindentation) or thermal treatment (i.e. artificial aging at intermediate temperatures), the excess elements and precipitates would be expelled out from the saturated (and unstable) solid solution and the solution becomes stable enhancing the strength of the alloy. Besides, the residual stresses, induced by water quenching, are responsible for enhanced strength in the WQ samples [59]. That is why the WQ structures provide the hardest and the second hardest states for the cast and the SLM materials. For the SLM material, the hardness values measured under as-built conditions are not exceeded for any of the combinations of temperature and time applied.

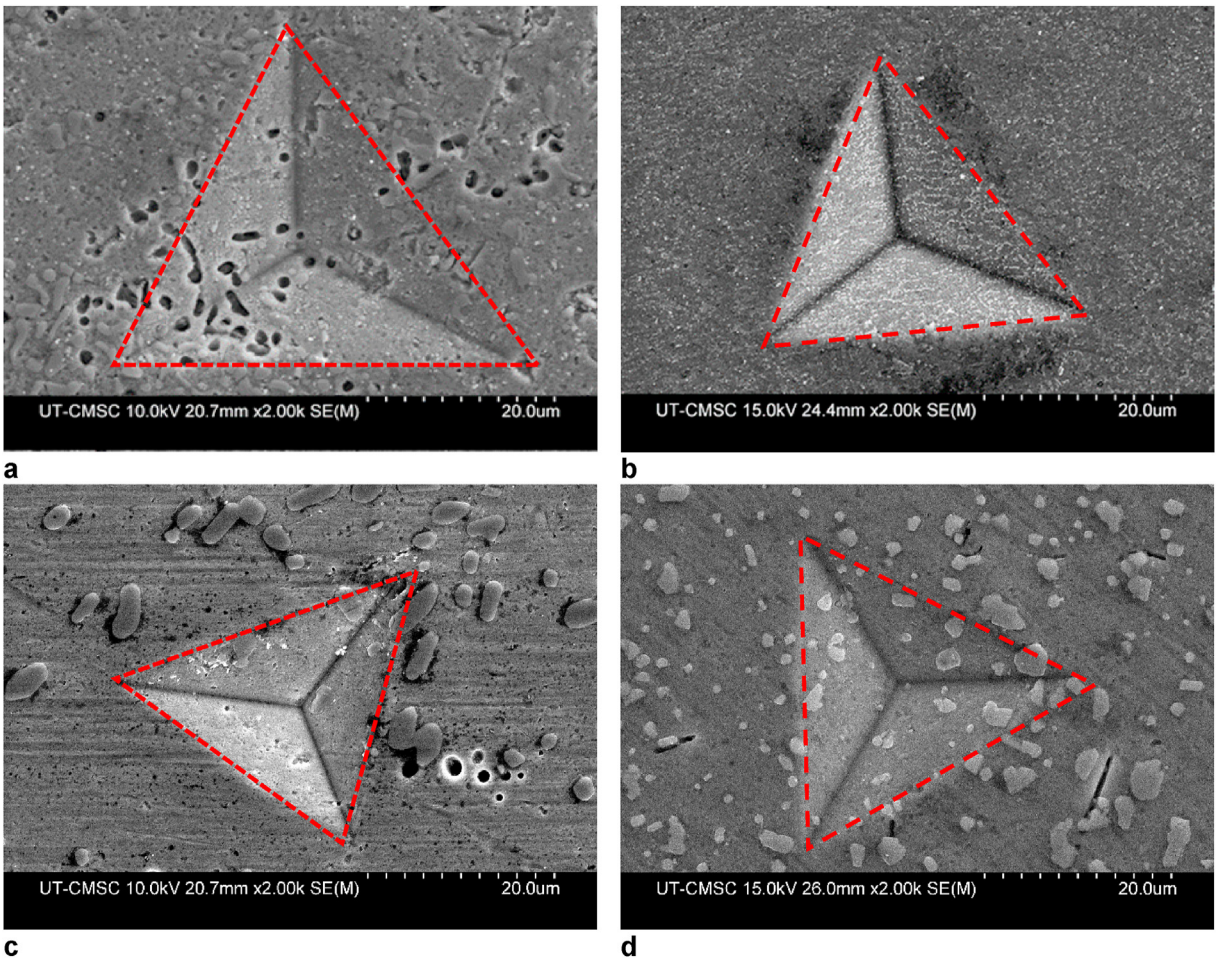

Fig. 17. The SEM micrographs showing indents on (a) as-cast; (b) as-printed; (c) WQ (cast); (d) WQ (SLM) AlSi10Mg samples.

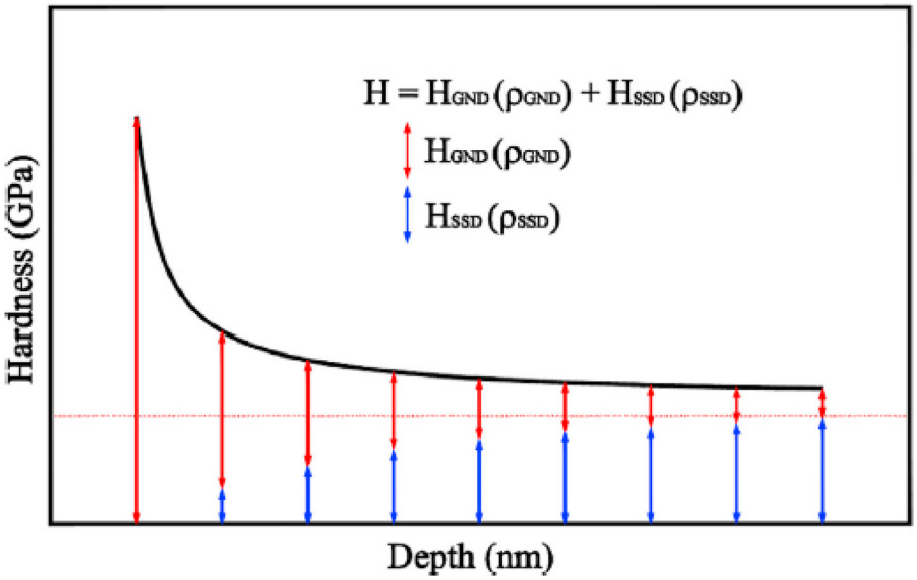

Fig. 18. Schematic plot of the ISE behavior and the contribution SSD and GND [69]. The dashed line shows the is the hardness due solely to statistically stored dislocations without the impact of geometrically necessary dislocations.

Solutionizing substantially reduces the hardness of the SLM materials and successive cooling with different rates (WQ to AC to FC) is not enough to exceed the values under conditions as built. Reduction in hardness upon solutionizing treatment of the SLM alloys is mainly due to the coarsening of the microstructure (grains) and eutectic-Si particles. That is, the very fine cellular structure that is obtained because of the

high solidification rate of the laser-assisted additive manufacturing is not maintained after solutionizing heat treatment thus causing a decrease in the mechanical strength of the alloy. The cellular network is destroyed, and eutectic-Si particles coarsen to some micrometer diameters. There might be some minor strengthening effect induced by solid-solution however the loss of the strength due to grain growth would prevail [27].

Upon heat treatment, with a decrease in the post-solutionizing cooling rate, more time would be available for the eutectic Si to spheroidize and eventually coarsen (grow). Through this transformation, the potential sites for stress concentration, e.g. sharp tips and corners of rod-like (fibrous) eutectic-Si are reduced [67,68]; hence, crack initiation is postponed and the plasticity (formability) index is improved; that is, the structure becomes more ductile. The cast WQ sample, with the highest hardness value, however, holds the least plasticity index.

As seen in Eq. (4), there is a direct relationship between wear resistance and hardness. For the SLM AlSi10Mg alloy, the as-built and the FC samples show the highest and lowest wear resistance, respectively. However, for the cast samples, changes in wear resistance is a bit different. The highest and lowest wear resistance was found at WQ and FC conditions, respectively for the cast AlSi10Mg alloy. The high wear resistance of the cast WQ samples is due to the high hardness of these samples induced by various mentioned strengthening mechanisms; i.e. solid solutions strengthening, and precipitation (Mg_2Si) hardening caused by post mechanical working (indentation). The least wear resistance belongs to the FC sample (in the cast and SLM conditions) which is the softest structure due to coarsening of the eutectic-Si particles and to some extent the coarsening of the aluminum grains.

The size of the indent becomes larger when the material becomes softer. Fig. 17 shows the indentation footprints in as fabricated and water quenched AlSi10Mg samples (both cast and SLM). In the as-fabricated condition, the indent size for the cast material is tangibly bigger than the indent size of the SLM part which means the SLM part is harder than its cast counterpart. In the water quenched condition, the scenario is opposite which means the WQ-SLM part is softer than its cast counterpart. The small indents observed in the as-fabricated SLM part and WQ cast part which is consistent with the nanoindentation results reported in Figs. 12 and 13.

The ISE is more pronounced at shallower indentation depths. This is because the material is almost dislocation free when the indenter depth is very low. The correlation between indentation stress and density of dislocations can be written as [69]:

$$\sigma_{ind} = 3\sqrt{3}\alpha G b\sqrt{\rho_{GND} + \rho_{SSD}} \tag{5}$$

where σ, α, G, b, ρ_{SSD}, ρ_{GND} are the flow stress, a material constant, the shear modulus, the Burgers vector, density of statistically stored dislocations (SSD) and density of geometrically necessary dislocations (GND), respectively. As presented in Eq. (5), both GNDs and SSDs contribute to indentation stress. Due to the low density of statistically stored dislocations (SSDs) existing around the indenter, the strength of the material is nearly as high as the theoretical strength. When the indenter further penetrates the material, geometrically necessary dislocations (GNDs) are generated. The multiplication of GNDs changes the strength and hardness of the material. With an increasing number of dislocations, their multiplication and mobility are impeded, thus the material experiences strain hardening. With increasing indenter depth, the indentation stress continuously diminishes and then reaches a rather steady-state plateau level (as seen in Fig. 14). The observed steady-state plateau in the indentation stress is due to the balance occurring between the dislocation multiplication and dislocation annihilation/rearrangement (in other words, the balance is between work hardening and dynamic recovery) [70–72]. The change in the contribution of dislocations as a function of depth is schematically shown in Fig. 18.

5. Summary

This research work is the first attempt to compare the structure and small-scale mechanical response of cast and SLM AlSi10Mg materials under specially designed post-fabrication heat treatments. In this paper, the effect of various post-fabrication thermal treatments on the microstructure and mechanical properties of cast and SLM AlSi10Mg alloy was investigated. The focus was to track the microstructural evolution (i.e., the morphology, size, distribution of eutectic Si in the microstructure, and texture) upon solutionizing and cooling at different media (e.g., water quenching, air cooling, and furnace cooling). To assess the correlation between microstructure and mechanical properties, a semi-destructive depth-sensing indentation testing technique was employed. To this end, indentation load-depth, indentation hardness, reduced modulus, and some quantitative parameters like plasticity index and WRI were extracted from the cast and SLM AlSi10Mg materials. The microstructural evolution was linked to the change in micromechanical properties of the studied cast and SLM AlSi10Mg alloys heat treated at different conditions.

The main findings of this study are given as follows:

(1) Among the materials at different conditions (as fabricated and heat-treated), the as-fabricated SLM and WQ-cast parts were found to be the hardest. The reason behind the superior hardness is the ultra-fine microstructure formed by extremely fast cooling rate induced during the process (as-fabricated SLM) and supersaturated structure by quenching and also the residual stress induced during the process in the cast alloy.
(2) Heat treatment significantly altered the microstructure and mechanical properties of the investigated materials.
(3) At furnace cooled condition, both SLM and cast parts were the softest. This is due to the slow cooling rate resulting in Si spheroidization and coarsening as well as grain growth.
(4) ISE was observed in both cast and SLM materials for all conditions.
(5) Si-particles in the heat-treated SLM materials are finer and further spheroidized compared with the heat-treated cast counter materials.
(6) The designed heat treatments did not change the texture of the SLM AlSi10Mg materials.

Credit author statement

S.I. Shakil:Writing – original draft. A. Hadadzadeh: Writing, review & editing, B. Shalchi Amirkhiz: Methodology. H. Pirgazi: Methodology. M. Mohammadi: Review & editing, M. Haghshenas: Conceptualization, Supervision.

Declaration of competing interest

The authors declare that they have no known competing financial interests or personal relationships that could have appeared to influence the work reported in this paper.

References

[1] H. Ye, An overview of the development of Al-Si-alloy based material for engine applications, J. Mater. Eng. Perform. 12 (3) (2003) 288–297.
[2] W. Li, S. Li, J. Liu, A. Zhang, Y. Zhou, Q. Wei, C. Yan, Y. Shi, Effect of heat treatment on AlSi10Mg alloy fabricated by selective laser melting: microstructure evolution, mechanical properties and fracture mechanism, Mater. Sci. Eng., A 663 (2016) 116–125.
[3] M. Hartlieb, Aluminum alloys for structural die casting, Die Cast. Eng. 57 (3) (2013) 40–43.
[4] H.R. Ammar, A.M. Samuel, F.H. Samuel, Porosity and the fatigue behavior of hypoeutectic and hypereutectic aluminum–silicon casting alloys, Int. J. Fatig. 30 (6) (2008) 1024–1035.
[5] K. Zyguła, B. Nosek, H. Pasiowiec, N. Szysiak, Mechanical properties and microstructure of AlSi10Mg alloy obtained by casting and SLM technique, World Scientific News 104 (2018) 462–472.

[6] A.H. Maamoun, Y.F. Xue, M.A. Elbestawi, S.C. Veldhuis, The effect of selective laser melting process parameters on the microstructure and mechanical properties of Al6061 and AlSi10Mg alloys, Materials 12 (1) (2019) 12.

[7] D. Du, J.C. Haley, A. Dong, Y. Fautrelle, D. Shu, G. Zhu, X. Li, B. Sun, E.J. Lavernia, Influence of static magnetic field on microstructure and mechanical behavior of selective laser melted AlSi10Mg alloy, Mater. Des. 181 (2019) 107923.

[8] N.T. Aboulkhair, M. Simonelli, L. Parry, I. Ashcroft, C. Tuck, R. Hague, 3D printing of Aluminium alloys: additive Manufacturing of Aluminium alloys using selective laser melting, Prog. Mater. Sci. 106 (2019) 100578.

[9] J. Zhang, B. Song, Q. Wei, D. Bourell, Y. Shi, A review of selective laser melting of aluminum alloys: processing, microstructure, property and developing trends, J. Mater. Sci. Technol. 35 (2) (2019) 270–284.

[10] SLM solutions GmbH. www.slm-solutions.com.

[11] E. Louvis, P. Fox, C.J. Sutcliffe, Selective laser melting of aluminium components, J. Mater. Process. Technol. 211 (2) (2011) 275–284.

[12] F. Trevisan, F. Calignano, M. Lorusso, J. Pakkanen, A. Aversa, E.P. Ambrosio, M. Lombardi, P. Fino, D. Manfredi, On the selective laser melting (SLM) of the AlSi10Mg alloy: process, microstructure, and mechanical properties, Materials 10 (1) (2017) 76.

[13] B. Zhang, H. Liao, C. Coddet, Effects of processing parameters on properties of selective laser melting Mg–9% Al powder mixture, Mater. Des. 34 (2012) 753–758.

[14] I. Rosenthal, A. Stern, N. Frage, Microstructure and mechanical properties of AlSi10Mg parts produced by the laser beam additive manufacturing, AM) technology, Metallography, Microstructure, and Analysis 3 (6) (2014) 448–453.

[15] J.Y. Wang, B.J. Wang, L.F. Huang, Structural evolution of Al–8% Si hypoeutectic alloy by ultrasonic processing, J. Mater. Sci. Technol. 33 (11) (2017) 1235–1239.

[16] A.M.A. Mohamed, A.M. Samuel, F.H. Samuel, H.W. Doty, Influence of additives on the microstructure and tensile properties of near-eutectic Al–10.8% Si cast alloy, Mater. Des. 30 (10) (2009) 3943–3957.

[17] F. Lv, L. Shen, H. Liang, D. Xie, C. Wang, Z. Tian, Mechanical properties of AlSi10Mg alloy fabricated by laser melting deposition and improvements via heat treatment, Optik 179 (2019) 8–18.

[18] N.T. Aboulkhair, A. Stephens, I. Maskery, C. Tuck, I. Ashcroft, N.M. Everitt, Mechanical Properties of Selective Laser Melted AlSi10Mg: Nano, Micro, and Macro Properties, pp. 1-30.

[19] L. Thijs, K. Kempen, J.-P. Kruth, J. Van Humbeeck, Fine-structured aluminium products with controllable texture by selective laser melting of pre-alloyed AlSi10Mg powder, Acta Mater. 61 (5) (2013) 1809–1819.

[20] N.T. Aboulkhair, C. Tuck, I. Ashcroft, I. Maskery, N.M. Everitt, On the precipitation hardening of selective laser melted AlSi10Mg, Metall. Mater. Trans. 46 (8) (2015) 3337–3341.

[21] N. Read, W. Wang, K. Essa, M.M. Attallah, Selective laser melting of AlSi10Mg alloy: process optimisation and mechanical properties development, Mater. Des. 65 (1980–2015) (2015) 417–424.

[22] F. Alghamdi, X. Song, A. Hadadzadeh, B. Shalchi-Amirkhiz, M. Mohammadi, M. Haghshenas, Post Heat Treatment of Additive Manufactured AlSi10Mg: on Silicon Morphology, Texture and Small-Scale Properties, Materials Science and Engineering: A, 2020, p. 139296.

[23] F. Alghamdi, M. Haghshenas, Microstructural and small-scale characterization of additive manufactured AlSi10Mg alloy, SN Applied Sciences 1 (3) (2019) 255.

[24] X.P. Li, G. Ji, Z. Chen, A. Addad, Y. Wu, H.W. Wang, J. Vleugels, J. Van Humbeeck, J.-P. Kruth, Selective laser melting of nano-TiB2 decorated AlSi10Mg alloy with high fracture strength and ductility, Acta Mater. 129 (2017) 183–193.

[25] B. Chen, S.K. Moon, X. Yao, G. Bi, J. Shen, J. Umeda, K. Kondoh, Strength and strain hardening of a selective laser melted AlSi10Mg alloy, Scripta Mater. 141 (2017) 45–49.

[26] E. Sjölander, S. Seifeddine, The heat treatment of Al–Si–Cu–Mg casting alloys, J. Mater. Process. Technol. 210 (10) (2010) 1249–1259.

[27] L. Girelli, M. Tocci, M. Gelfi, A. Pola, Study of heat treatment parameters for additively manufactured AlSi10Mg in comparison with corresponding cast alloy, Mater. Sci. Eng., A 739 (2019) 317–328.

[28] L. Girelli, M. Tocci, L. Montesano, M. Gelfi, A. Pola, Optimization of heat treatment parameters for additive manufacturing and gravity casting AlSi10Mg alloy.

[29] L. Girelli, M. Tocci, M. Conte, R. Giovanardi, P. Veronesi, M. Gelfi, A. Pola, Effect of the T6 heat treatment on corrosion behavior of additive manufactured and gravity cast AlSi10Mg alloy, Mater. Corros. 70 (10) (2019) 1808–1816.

[30] M.A. Moustafa, F.H. Samuel, H.W. Doty, Effect of solution heat treatment and additives on the microstructure of Al-Si (A413. 1) automotive alloys, J. Mater. Sci. 38 (22) (2003) 4507–4522.

[31] L. Zhou, A. Mehta, E. Schulz, B. McWilliams, K. Cho, Y. Sohn, Microstructure, precipitates and hardness of selectively laser melted AlSi10Mg alloy before and after heat treatment, Mater. Char. 143 (2018) 5–17.

[32] X.P. Li, X.J. Wang, M. Saunders, A. Suvorova, L.C. Zhang, Y.J. Liu, M.H. Fang, Z.H. Huang, T.B. Sercombe, A selective laser melting and solution heat treatment refined Al–12Si alloy with a controllable ultrafine eutectic microstructure and 25% tensile ductility, Acta Mater. 95 (2015) 74–82.

[33] Metal Working World Magazine, Foundry vs Additive Comparison of Performances and Heat Treatments for an Al-Si-Mg Alloy, 2019. https://www.metalworkingworldmagazine.com/foundry-vs-additive-comparison-of-performances-and-heat-treatments-for-an-al-si-mg-alloy/.

[34] N.T. Aboulkhair, C. Tuck, I. Ashcroft, I. Maskery, N.M.J.M. Everitt, M.T. A, On the precipitation hardening of selective laser melted, AlSi10Mg 46 (8) (2015) 3337–3341.

[35] J. Fite, S.E. Prameela, J.A. Slotwinski, T.P. Weihs, Evolution of the microstructure and mechanical properties of additively manufactured AlSi10Mg during room temperature holds and low temperature aging, Additive Manufacturing 36 (2020) 101429.

[36] M. Albu, R. Krisper, J. Lammer, G. Kothleitner, J. Fiocchi, P. Bassani, Microstructure evolution during in-situ heating of Alsi10Mg alloy powders and additive manufactured parts, Additive Manufacturing 36 (2020) 101605.

[37] M. Ibrahim, M. Abdelaziz, A. Samuel, H. Doty, F. Samuel, Spheroidization and coarsening of eutectic Si particles in Al-Si-based alloys, Advances in Materials Science and Engineering (2021).

[38] A. Iturrioz, E. Gil, M.M. Petite, F. Garciandia, A.M. Mancisidor, M. San Sebastian, Selective laser melting of AlSi10Mg alloy: influence of heat treatment condition on mechanical properties and microstructure, Weld. World 62 (4) (2018) 885–892.

[39] A. Hadadzadeh, B.S. Amirkhiz, A. Odeshi, J. Li, M. Mohammadi, Role of hierarchical microstructure of additively manufactured AlSi10Mg on dynamic loading behavior, Additive Manufacturing 28 (2019) 1–13.

[40] J. Hay, Introduction to instrumented indentation testing, Exp. Tech. 33 (6) (2009) 66–72.

[41] W.C. Oliver, G.M. Pharr, An improved technique for determining hardness and elastic modulus using load and displacement sensing indentation experiments, J. Mater. Res. 7 (6) (1992) 1564–1583.

[42] A. Hadadzadeh, C. Baxter, B.S. Amirkhiz, M. Mohammadi, Strengthening mechanisms in direct metal laser sintered AlSi10Mg: comparison between virgin and recycled powders, Additive Manufacturing 23 (2018) 108–120.

[43] M.H. Abdelaziz, A.M. Samuel, H.W. Doty, F.H. Samuel, Effect of morphological changes of eutectic Si particles on the ambient and high temperature tensile properties of Zr containing Al–Si alloys, Journal of Materials Research and Technology (2020).

[44] Z. Li, Z. Kuai, P. Bai, Y. Nie, G. Fu, W. Liu, S. Yang, Microstructure and tensile properties of AlSi10Mg alloy manufactured by multi-laser beam selective laser melting (SLM), Metals 9 (12) (2019) 1337.

[45] X. Liu, C. Zhao, X. Zhou, Z. Shen, W. Liu, Microstructure of selective laser melted AlSi10Mg alloy, Mater. Des. 168 (2019) 107677.

[46] X. Wu, H. Zhang, H. Jiang, Z. Mi, H. Zhang, Multi-refinement effect of rare earth lanthanum on α-Al and eutectic Si phase in hypoeutectic Al-7Si alloy, Metals 10 (5) (2020) 621.

[47] M. Muhammad, J.W. Pegues, N. Shamsaei, M. Haghshenas, Effect of heat treatments on microstructure/small-scale properties of additive manufactured Ti-6Al-4V, Int. J. Adv. Manuf. Technol. 103 (9–12) (2019) 4161–4172.

[48] J. Thornby, D. Verma, R. Cochrane, A. Westwood, V.B. Manakari, M. Gupta, M. Haghshenas, Indentation-based characterization of creep and hardness behavior of magnesium carbon nanotube nanocomposites at room temperature, SN Applied Sciences 1 (7) (2019) 695.

[49] M. Haghshenas, R.J. Klassen, Assessment of the depth dependence of the indentation stress during constant strain rate nanoindentation of 70/30 brass, Mater. Sci. Eng., A 572 (2013) 91–97.

[50] A. Karimzadeh, M.R. Ayatollahi, Mechanical Properties of Biomaterials Determined by Nano-Indentation and Nano-Scratch Tests, Nanomechanical Analysis of High Performance Materials, Springer, 2014, pp. 189–207.

[51] B.J. Briscoe, L. Fiori, E. Pelillo, Nano-indentation of polymeric surfaces, J. Phys. Appl. Phys. 31 (19) (1998) 2395.

[52] D. Labonte, A.-K. Lenz, M.L. Oyen, On the relationship between indentation hardness and modulus, and the damage resistance of biological materials, Acta Biomater. 57 (2017) 373–383.

[53] G. Pintaude, Introduction of the Ratio of the Hardness to the Reduced Elastic Modulus for Abrasion, Tribology-Fundamentals and Advancements, IntechOpen2013.

[54] Y.C. Lin, S.-C. Luo, J. Huang, L.-X. Yin, X.-Y. Jiang, Effects of solution treatment on microstructures and micro-hardness of a Sr-modified Al-Si-Mg alloy, Mater. Sci. Eng., A 725 (2018) 530–540.

[55] Q. Li, F. Li, T. Xia, Y. Lan, Y. Jian, F. Tao, Effects of in-situ γ-Al2O3 particles and heat treatment on the microstructure and mechanical properties of A356 aluminium alloy, J. Alloys Compd. 627 (2015) 352–358.

[56] C.-l. Yang, Y.-b. Li, D. Bo, H.-b. Lue, L.I.U. Feng, Effects of cooling rate on solution heat treatment of as-cast A356 alloy, Trans. Nonferrous Metals Soc. China 25 (10) (2015) 3189–3196.

[57] K. Kempen, L. Thijs, J. Van Humbeeck, J.-P.J.P.P. Kruth, Mechanical properties of AlSi10Mg produced by selective laser melting 39 (2012) 439–446.

[58] J. Zou, Y. Zhu, M. Pan, T. Xie, X. Chen, H. Yang, A study on cavitation erosion behavior of AlSi10Mg fabricated by selective laser melting (SLM), Wear 376 (2017) 496–506.

[59] E. Padovano, C. Badini, A. Pantarelli, F. Gili, F. D'Aiuto, A comparative study of the effects of thermal treatments on AlSi10Mg produced by laser powder bed fusion, J. Alloys Compd. (2020) 154822.

[60] M. Zamani, Al-Si Cast Alloys-Microstructure and Mechanical Properties at Ambient and Elevated Temperatures, Jönköping University, School of Engineering, 2017.

[61] J. Wu, X. Wang, W. Wang, M. Attallah, M.J.A.M. Loretto, Microstructure and strength of selectively laser melted, AlSi10Mg 117 (2016) 311–320.

[62] T. Maeshima, K. Oh-ishi, Solute clustering and supersaturated solid solution of AlSi10Mg alloy fabricated by selective laser melting, Heliyon 5 (2) (2019), e01186.

[63] P. Wei, Z. Wei, Z. Chen, J. Du, Y. He, J. Li, Y. Zhou, The AlSi10Mg samples produced by selective laser melting: single track, densification, microstructure and mechanical behavior, Appl. Surf. Sci. 408 (2017) 38–50.

[64] L.J. Colley, M.A. Wells, W.J. Poole, Microstructure–strength models for heat treatment of Al–Si–Mg casting alloys I: microstructure evolution and precipitation kinetics, Canadian Metallurgical Quarterly 53 (2) (2014) 125–137.

[65] D. Apelian, S. Shivkumar, G. Sigworth, Fundamental aspects of heat treatment of cast Al-Si-Mg alloys, AFS transactions 97 (1989) 727–742.

[66] D.L. Zhang, L. Zheng, The quench sensitivity of cast Al-7 wt pct Si-0.4 wt pct Mg alloy, Metall. Mater. Trans. 27 (12) (1996) 3983–3991.
[67] A. Malekan, M. Emamy, J. Rassizadehghani, A.R. Emami, The effect of solution temperature on the microstructure and tensile properties of Al–15% Mg2Si composite, Mater. Des. 32 (5) (2011) 2701–2709.
[68] M. Zhu, Z. Jian, G. Yang, Y. Zhou, Effects of T6 heat treatment on the microstructure, tensile properties, and fracture behavior of the modified A356 alloys, Mater. Des. 36 (1980–2015) (2012) 243–249.
[69] N.-V. Nguyen, S.-E. Kim, Experimental study to investigate microstructure and continuous strain rate sensitivity of structural steel weld zone using nanoindentation, Int. J. Mech. Sci. 174 (2020) 105482.
[70] M. Muhammad, M. Masoomi, B. Torries, N. Shamsaei, M. Haghshenas, Depth-sensing time-dependent response of additively manufactured Ti-6Al-4V alloy, Additive Manufacturing 24 (2018) 37–46.
[71] S. Mohd Yusuf, Y. Chen, S. Yang, N. Gao, Micromechanical response of additively manufactured 316L stainless steel processed by high-pressure torsion, Adv. Eng. Mater. 22 (10) (2020) 2000052.
[72] S.I. Shakil, C. Dharmendra, B.S. Amirkhiz, D. Verma, M. Mohammadi, M. Haghshenas, Micromechanical Characterization of Wire-Arc Additive Manufactured and Cast Nickel Aluminum Bronze: Ambient and Intermediate Temperatures, Materials Science and Engineering: A, 2020, p. 139773.